

Research paper

Vibration suppression for post-capture spacecraft via a novel bio-inspired Stewart isolation system

Xin Wang^{a,b,*}, Xiaokui Yue^{a,b,**}, Honghua Dai^{a,b}, Jianping Yuan^{a,b}^a National Key Laboratory of Aerospace Flight Dynamics, Northwestern Polytechnical University, Xi'an, China^b School of Astronautics, Northwestern Polytechnical University, Xi'an, China

ARTICLE INFO

Keywords:

On-orbit capture
Vibration suppression
X-shape structure
Stewart platform
ADAMS

ABSTRACT

In the process of on-orbit capture mission, some undesirable vibrations arising from the relative motions between the servicing spacecraft and the target are inevitable, which can make the post-capture combined spacecraft unstable or even tumbling. Therefore, suppressing post-capture vibrations is critical to mission success. In this work, a novel bio-inspired X-shape structure-based Stewart isolation platform (XSSIP) system is first proposed to install between the satellite platform and the capture mechanism. It can suppress the post-capture vibrations of a free-floating spacecraft subjected to the impulsive or periodic external forces. Beneficial nonlinear stiffness and nonlinear damping characteristics with the existence of X-shape structure can be acquired, which is helpful to achieve much better vibration isolation performance in multiple directions. Different from the traditional ground vibration isolation system, the dynamic equations of the 6-DOF under-constrained system in the weightless environment of space are established by Lagrange's principle. Influences on vibration isolation performance of the XSSIP system incurred by different structural parameters are systematically studied under either periodic or impulsive excitations. In addition, ADAMS simulation is conducted to verify the accuracy and feasibility of the theoretical model. Compared with the traditional spring-mass-damper (SMD)-based Stewart isolation platform system, the XSSIP system possesses an obvious advantage and offers a highly efficient passive way for suppressing post-capture vibrations of the floating spacecraft.

1. Introduction

Vibration exists widely in all fields and presents a critical issue in engineering practices, such as protection of high precision instruments [1,2], vehicle ride comfort improvement [3] and on-orbit vibration suppression of spacecraft [4,5]. With the rapid development of space technology, on-orbit servicing (OOS) [6] is becoming a new trend in the past two decades. It will be popular to conduct on-orbit assembly [7], on-orbit maintenance [8], refueling [9] and retrieval [10] of malfunctioning satellites in future space operations. For instance, SMART-OLEV [11] and FREND [12] were launched to supply the on-orbit spacecraft with propulsion, navigation and guidance services to extend their operational lifetime. Among them, on-orbit capture as the key technology has attracted extensive attentions owing to its intriguing and potential military, civil and commercial applications in the future space missions. Especially in the process of capturing some non-cooperative targets including malfunctioning satellites [13] and space debris [14] that lack partial or full state information, there always exists

an impact between the capture mechanism and the target. It can lead to some undesirable vibrations and drift motions for the satellite platform [15]. The induced vibrations can damage the sensitive payloads mounted on the satellite platform of spacecraft, which makes them not function well. Therefore, the post-capture vibration suppression is vital to ensure the stability and safety of the combined spacecraft.

Generally, the forced vibrations can be classified into two types according to the differences of vibration sources operating the capture missions. One is the periodic excitation, which mainly arises from the moving payloads mounted on the target, such as the driving mechanism of solar panel, the reaction flywheel and the propulsion. The other is from the collisions with the target, such as the spacecraft waiting for service or space debris [16]. For the non-cooperative target, this kind of collisions may be very strong, which can do damage to the pointing accuracy and performance of precise instruments.

Nevertheless, when dealing with the post-capture combined spacecraft, the servicing spacecraft and the target are always thought as rigidly connected without relative motions in the existing literature.

* Corresponding author

** Corresponding author

E-mail addresses: wangxin1989@mail.nwpu.edu.cn (X. Wang), xkyue@nwpu.edu.cn (X. Yue), hhdai@nwpu.edu.cn (H. Dai), jyuan@nwpu.edu.cn (J. Yuan).

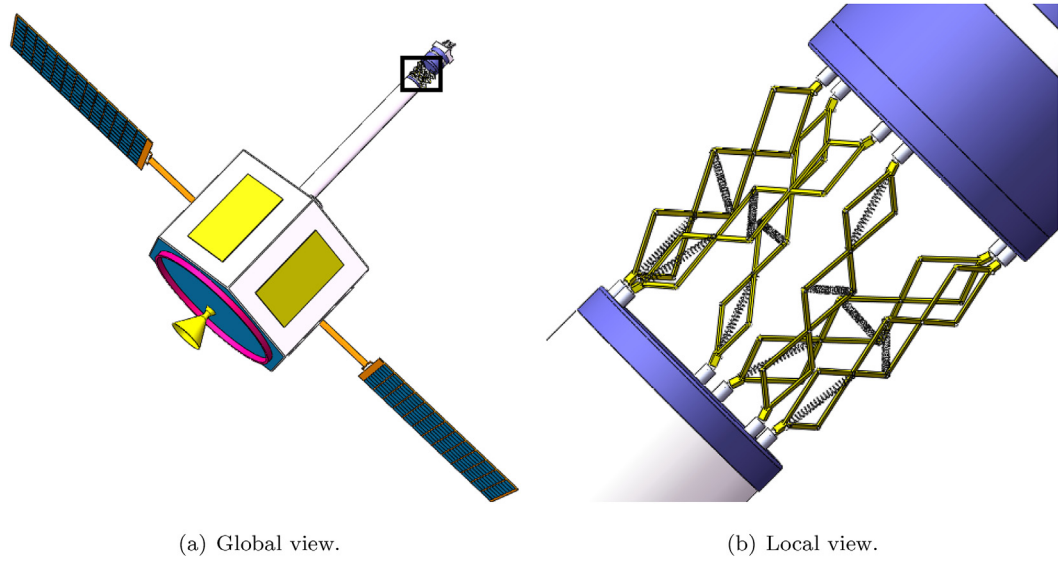


Fig. 1. Schematic diagram of an on-orbit capture mission with the XSSIP system.

Under this circumstance, neglecting the relative motions would make the post-capture combination unstable or even tumbling. In this case, Dai et al. [17,18] proposed a novel loosely connected pattern, where a bio-inspired X-shape isolator is used to cope with the impact between the chaser and the target. The kind of bio-inspired X-shape structure inspired from the limb structures of birds in motion vibration isolation and suppression was proposed and studied in Refs. [19–22]. The excellent high-static-low-dynamic stiffness property can be achieved by flexibly designing the structural parameters. Similarly, very excellent vibration isolation performance can be obtained through the application of the loosely connected model. However, Refs. [17,18] only considered the axial vibration suppression of the bio-inspired structure system. Hence it cannot be applied to the on-orbit capture mission wherein multi-direction vibrations exist. To achieve multi-direction vibration isolation, multi-DOF isolators have been investigated by applying various materials and structure designs. The Stewart platform [23,24] is a commonly employed mechanism to realize multi-DOF vibration isolation [25–29] and widely used in the space area [30–32], which consists of two platforms and six extensible legs as the supporting structure. Based on the nonlinear stiffness and damping property of the X-shape structure and the characteristics of Stewart platform, a novel six-DOF vibration isolator [25] was investigated by following a Stewart platform configuration but applying the bio-inspired X-shape structure as legs, which can realize passive vibration isolation performance without losing loading capacity in six directions. However, this type of Stewart platform cannot apply in the present on-orbit capture problem, because the platform is fixed to the ground and cannot simulate the case in under-constrained space environment. Therefore, the anti-impact model in the capture operation needs to be established.

In this work, the passive XSSIP system inspired by the foregoing discussions is first proposed to install between the robotic arm and the capture mechanism of spacecraft to suppress vibrations when subjected to the impulsive or periodic external forces. And the XSSIP system is an under-constrained multi-DOF system, in which each leg of the Stewart platform is substituted by the n -layer X-shape structure. In the meantime, when the manipulator of spacecraft captures the target, the tangential and normal vibrations are frequently encountered, which will be investigated in this work later. The dynamical model of the XSSIP system in the weightless environment of space is established by Lagrange's principle for the case under the impulsive or periodic external excitations. The vibration isolation performance of the XSSIP system is verified by comparing with the conventional SMD-based Stewart isolation platform system. Theoretical analyses demonstrate

that the XSSIP system has a far better vibration isolation performance. In summary, the contributions of our work are threefold:

\mathcal{C}_1 A kind of X-shape structure-based Stewart isolation platform system is first proposed and installed between the robotic arm and the capture mechanism to suppress the post-capture vibrations of free-floating spacecraft.

\mathcal{C}_2 Different from the traditional ground vibration isolation system, the dynamical model of the XSSIP system in the weightless environment of space is established to simulate the post-capture dynamical response.

\mathcal{C}_3 The ADAMS simulations are conducted for the 6-DOF under-constrained system under the impact and periodic external excitations to verify the accuracy and feasibility of the XSSIP model.

This paper is arranged as follows. In section 2, the XSSIP system between the satellite platform and the robotic arm of spacecraft is presented in on-orbit capture missions. The dynamical model of the XSSIP system is established in section 3. The vibration isolation performances of the present system are studied under the impulsive and periodic external excitations in sections 4 and 5, where influences on the isolation performance with respect to different structural parameters are investigated in detail. The ADAMS simulations of the XSSIP system are conducted to verify the accuracy of the dynamical model in section 6. Finally, a conclusion in section 7 is drawn to summarize the results.

2. The X-shape structure-based Stewart isolation platform

The schematic diagram of on-orbit capture mission with the XSSIP system is presented in Fig. 1. The X-shape structure-based Stewart isolation platform is shown separately in Fig. 2, whose initial height is H . The XSSIP system contains two platforms that we call the left platform and the right platform later and six equal X-shape supporting structures. From this figure, we can see that the left platform is connected to the robotic arm of spacecraft and the capture mechanism is mounted on the right platform, respectively. Two coordinate systems $O_1 - X_1 Y_1 Z_1$ and $O_2 - X_2 Y_2 Z_2$ are established at the centers of two platforms. L_j is the connection point on the left platform and R_j is that on the right platform for the i -th leg. For the purpose of simplicity, we number the six legs as $\Pi_i (i = 1, \dots, 6)$, which are labeled in Fig. 3 detailedly. The location of the connecting point R_j on the coordinate system $O_1 - X_1 Y_1 Z_1$ is written as follows:

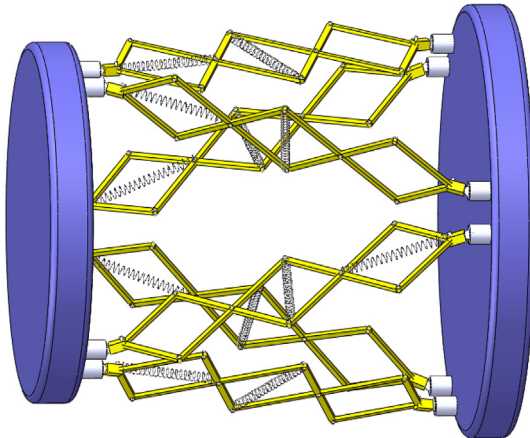


Fig. 2. Schematic diagram of the XSSIP system.

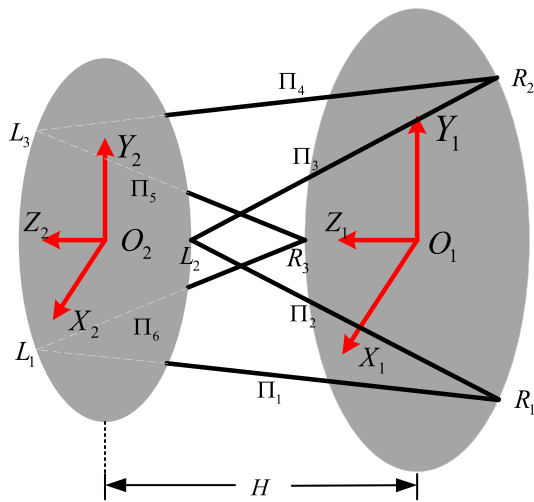


Fig. 3. The leg-labeled diagram of the XSSIP system.

$$R_j = \begin{bmatrix} r_1 \cos(\Xi_{1,j}) \\ r_1 \sin(\Xi_{1,j}) \\ 0 \end{bmatrix}, \quad \Xi_{1,j} = \frac{\pi}{3}(2j-1), \quad j = 1, 2, 3. \quad (1)$$

where r_1 is the radius of the right platform. Similarly, the location of the connecting point L_j on the coordinate system $O_2 - X_2 Y_2 Z_2$ has the same form:

$$L_j = \begin{bmatrix} r_2 \cos(\Xi_{2,j}) \\ r_2 \sin(\Xi_{2,j}) \\ 0 \end{bmatrix}, \quad \Xi_{2,j} = \frac{2\pi}{3}(j-1), \quad j = 1, 2, 3. \quad (2)$$

where r_2 is the radius of the left platform.

The “leg” of the Stewart platform – the supporting structure is constructed by a bio-inspired n -layer X-shape structure, which is shown in Fig. 4 with the rod length L and the original assembly angle θ . Each layer contains four rods and four joints, whose masses are always neglected in that they are much smaller than the mass of platform. k_1 and k_2 denote the horizontal and vertical spring stiffness coefficient, respectively. The geometrical relationship between the initial and deformed configurations is shown in Fig. 5. The deformation of the X-shape structure can be expressed as

$$\tan(\theta - \phi_i) = \frac{L \sin \theta - \frac{q_i}{2n}}{L \cos \theta + \frac{s_i}{2}} \quad (3)$$

$$L^2 = \left(L \sin \theta - \frac{q_i}{2n} \right)^2 + \left(L \cos \theta + \frac{s_i}{2} \right)^2 \quad (4)$$

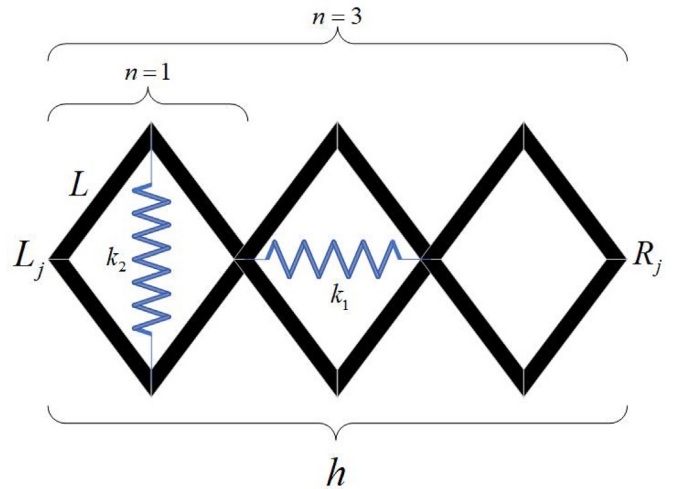


Fig. 4. The schematic structure of one supporting leg – the three-layer X-shape structure.

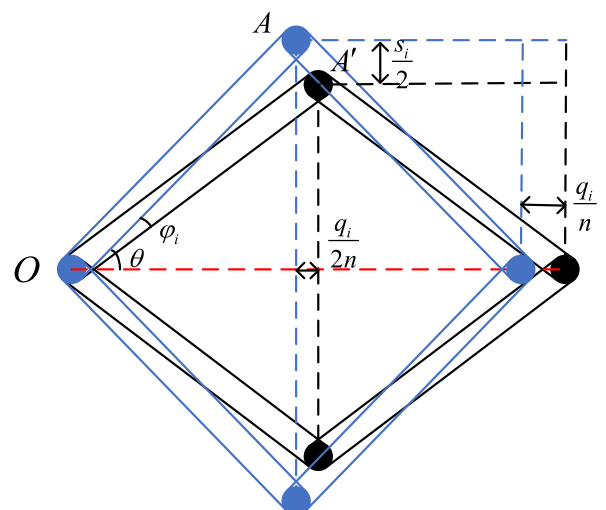


Fig. 5. The initial (black) and deformed (blue) states of the X-shape structure. (For interpretation of the references to colour in this figure legend, the reader is referred to the Web version of this article.)

where q_i represents the horizontal motion of the connecting point and s_i is the vertical motion of the connecting joint A . ϕ_i denotes the rotation angle of the rod OA for the i -th leg and θ is the initial assembly angle, respectively. The geometrical relationship of the spatial vectors for the i -th leg is shown in Fig. 6, which is marked as the red line.

To describe the relationship of vectors better, we regard the right coordinate system as the main coordinate one. According to the geometrical relationship of the spatial vectors, we can obtain

$$\Psi_i = L'_j + \hat{P} - R_j \quad (i = 1, \dots, 6, j = 1, 2, 3) \quad (5)$$

where $L'_j = L_j + [0, 0, H]^T$, L_j and R_j have been given before. $\hat{P} = [\hat{x}, \hat{y}, \hat{z} + H]^T$, \hat{x} , \hat{y} and \hat{z} are the relative motions of the left platform with respect to the right platform, respectively. The initial length of n -layer X-shape structure is $h = 2nL \sin \theta$ and the deformed length of the i -th leg is expressed by $|\Psi_i|$. From above, some related equations can be obtained as follows.

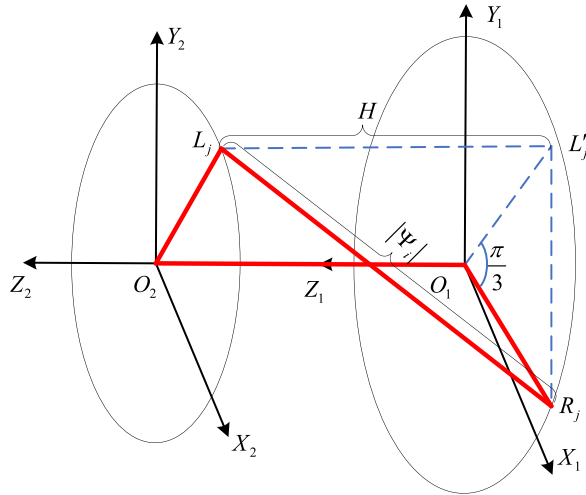


Fig. 6. The geometrical relationship of the spatial vectors for the i -th leg.

$$\begin{aligned} q_i &= h - |\Psi_i| = 2nL\sin\theta - |\Psi_i| \\ s_i &= 2\sqrt{L^2 - \left(L\sin\theta - \frac{q_i}{2n}\right)^2} - 2L\cos\theta = \frac{1}{n}\sqrt{4n^2L^2 - |\Psi_i|^2} - 2L\cos\theta \\ \phi_i &= \theta - \arctan\left(\frac{L\sin\theta - \frac{q_i}{2n}}{L\cos\theta + \frac{s_i}{2}}\right) = \theta - \arctan\left(\frac{|\Psi_i|}{\sqrt{4n^2L^2 - |\Psi_i|^2}}\right) \end{aligned} \quad (6)$$

3. Establishment of the dynamic equations

The XSSIP system in this paper includes two platforms: the left and right platforms, several rods, rotating joints and springs. As mentioned earlier, the masses of rods and joints are always neglected in that they are much lighter than any one of platforms. Therefore, the kinetic energy is represented as:

$$T = \frac{1}{2}m_1(\dot{x}_1^2 + \dot{y}_1^2 + \dot{z}_1^2) + \frac{1}{2}m_2(\dot{x}_2^2 + \dot{y}_2^2 + \dot{z}_2^2) \quad (7)$$

where m_1 represents the mass of the right platform, the target and capturing mechanism, m_2 stands for the mass of the left platform, the robotic arm and the satellite platform.

The potential energy is denoted as follows:

$$V = \frac{1}{2}k_1 \sum_{i=1}^6 \left(\frac{q_i}{n}\right)^2 + \frac{1}{2}k_2 \sum_{i=1}^6 s_i^2 \quad (8)$$

where q_i and s_i are described as earlier in detail, k_1 and k_2 are the stiffness coefficients of horizontal and vertical springs, respectively.

The virtual work by non-conservative forces for the i -th leg of the XSSIP system is obtained as

$$\delta W_i = -2(3n+1)c\dot{\phi}_i\delta\phi_i - c_1\hat{x}\delta\hat{x} - c_2\hat{y}\delta\hat{y} - c_3\hat{z}\delta\hat{z} \quad (i = 1, \dots, 6) \quad (9)$$

where c is the rotating friction coefficient of each joint and c_i ($i = 1, 2, 3$) is the air damping coefficient in each direction.

$$\begin{aligned} \delta W_i &= \left[-2(3n+1)c\dot{\phi}_i\frac{\partial\phi_i}{\partial x_1} + c_1(\dot{x}_2 - \dot{x}_1) \right] \delta x_1 \\ &\quad + \left[-2(3n+1)c\dot{\phi}_i\frac{\partial\phi_i}{\partial x_2} - c_1(\dot{x}_2 - \dot{x}_1) \right] \delta x_2 \\ &\quad + \left[-2(3n+1)c\dot{\phi}_i\frac{\partial\phi_i}{\partial y_1} + c_2(\dot{y}_2 - \dot{y}_1) \right] \delta y_1 \\ &\quad + \left[-2(3n+1)c\dot{\phi}_i\frac{\partial\phi_i}{\partial y_2} - c_2(\dot{y}_2 - \dot{y}_1) \right] \delta y_2 \\ &\quad + \left[-2(3n+1)c\dot{\phi}_i\frac{\partial\phi_i}{\partial z_1} + c_3(\dot{z}_2 - \dot{z}_1) \right] \delta z_1 \\ &\quad + \left[-2(3n+1)c\dot{\phi}_i\frac{\partial\phi_i}{\partial z_2} - c_3(\dot{z}_2 - \dot{z}_1) \right] \delta z_2 \\ &= \sum_{j=1}^6 \Sigma_j \delta \Delta_j \end{aligned} \quad (10)$$

where Σ_j ($j = 1, \dots, 6$) and Δ_j ($j = 1, \dots, 6$) represent the generalized forces and the generalized coordinates, respectively.

Therefore, the whole virtual work of the XSSIP system can be obtained as follows

$$\delta W = \sum_{i=1}^6 \delta W_i \quad (11)$$

The dynamic equations of the XSSIP system can be established by Lagrange's principle

$$\frac{d}{dt} \left(\frac{\partial U}{\partial \dot{\Delta}_i} \right) - \frac{\partial U}{\partial \Delta_i} = \Sigma_i \quad (12)$$

where $U = T - V$ is referred to as the Lagrange function. Therefore, the dynamic equations can be obtained as follows:

$$\begin{aligned} m_1\ddot{x}_1 + \frac{k_1}{n^2} \sum_{i=1}^6 q_i \frac{\partial q_i}{\partial x_1} + k_2 \sum_{i=1}^6 s_i \frac{\partial s_i}{\partial x_1} &= \sum_{i=1}^6 \left[-2(3n+1)c\dot{\phi}_i\frac{\partial\phi_i}{\partial x_1} + c_1(\dot{x}_2 - \dot{x}_1) \right] \\ m_2\ddot{x}_2 + \frac{k_1}{n^2} \sum_{i=1}^6 q_i \frac{\partial q_i}{\partial x_2} + k_2 \sum_{i=1}^6 s_i \frac{\partial s_i}{\partial x_2} &= \sum_{i=1}^6 \left[-2(3n+1)c\dot{\phi}_i\frac{\partial\phi_i}{\partial x_2} - c_1(\dot{x}_2 - \dot{x}_1) \right] \\ m_1\ddot{y}_1 + \frac{k_1}{n^2} \sum_{i=1}^6 q_i \frac{\partial q_i}{\partial y_1} + k_2 \sum_{i=1}^6 s_i \frac{\partial s_i}{\partial y_1} &= \sum_{i=1}^6 \left[-2(3n+1)c\dot{\phi}_i\frac{\partial\phi_i}{\partial y_1} + c_2(\dot{y}_2 - \dot{y}_1) \right] \\ m_2\ddot{y}_2 + \frac{k_1}{n^2} \sum_{i=1}^6 q_i \frac{\partial q_i}{\partial y_2} + k_2 \sum_{i=1}^6 s_i \frac{\partial s_i}{\partial y_2} &= \sum_{i=1}^6 \left[-2(3n+1)c\dot{\phi}_i\frac{\partial\phi_i}{\partial y_2} - c_2(\dot{y}_2 - \dot{y}_1) \right] \\ m_1\ddot{z}_1 + \frac{k_1}{n^2} \sum_{i=1}^6 q_i \frac{\partial q_i}{\partial z_1} + k_2 \sum_{i=1}^6 s_i \frac{\partial s_i}{\partial z_1} &= \sum_{i=1}^6 \left[-2(3n+1)c\dot{\phi}_i\frac{\partial\phi_i}{\partial z_1} + c_3(\dot{z}_2 - \dot{z}_1) \right] \\ m_2\ddot{z}_2 + \frac{k_1}{n^2} \sum_{i=1}^6 q_i \frac{\partial q_i}{\partial z_2} + k_2 \sum_{i=1}^6 s_i \frac{\partial s_i}{\partial z_2} &= \sum_{i=1}^6 \left[-2(3n+1)c\dot{\phi}_i\frac{\partial\phi_i}{\partial z_2} - c_3(\dot{z}_2 - \dot{z}_1) \right] \end{aligned} \quad (13)$$

The above equations can be written as the following forms:

$$\begin{aligned}
m_1 \ddot{x}_1 - \frac{k_1}{n^2} \sum_{i=1}^6 (2nL\sin\theta - |\Psi_i|) \frac{\partial |\Psi_i|}{\partial x_1} - \frac{k_2}{n^2} \sum_{i=1}^6 \left(1 - \frac{2nL\cos\theta}{\sqrt{4n^2L^2 - |\Psi_i|^2}} \right) |\Psi_i| \\
\left| \frac{\partial |\Psi_i|}{\partial x_1} \right| = \sum_{i=1}^6 \left[-2(3n+1)c\dot{\phi}_i \right] \\
m_2 \ddot{x}_2 - \frac{k_1}{n^2} \sum_{i=1}^6 (2nL\sin\theta - |\Psi_i|) \frac{\partial |\Psi_i|}{\partial x_2} - \frac{k_2}{n^2} \sum_{i=1}^6 \left(1 - \frac{2nL\cos\theta}{\sqrt{4n^2L^2 - |\Psi_i|^2}} \right) |\Psi_i| \\
\left| \frac{\partial |\Psi_i|}{\partial x_2} \right| = \sum_{i=1}^6 \left[-2(3n+1)c\dot{\phi}_i \right] \\
m_1 \ddot{y}_1 - \frac{k_1}{n^2} \sum_{i=1}^6 (2nL\sin\theta - |\Psi_i|) \frac{\partial |\Psi_i|}{\partial y_1} - \frac{k_2}{n^2} \sum_{i=1}^6 \left(1 - \frac{2nL\cos\theta}{\sqrt{4n^2L^2 - |\Psi_i|^2}} \right) |\Psi_i| \\
\left| \frac{\partial |\Psi_i|}{\partial y_1} \right| = \sum_{i=1}^6 \left[-2(3n+1)c\dot{\phi}_i \right] \\
m_2 \ddot{y}_2 - \frac{k_1}{n^2} \sum_{i=1}^6 (2nL\sin\theta - |\Psi_i|) \frac{\partial |\Psi_i|}{\partial y_2} - \frac{k_2}{n^2} \sum_{i=1}^6 \left(1 - \frac{2nL\cos\theta}{\sqrt{4n^2L^2 - |\Psi_i|^2}} \right) |\Psi_i| \\
\left| \frac{\partial |\Psi_i|}{\partial y_2} \right| = \sum_{i=1}^6 \left[-2(3n+1)c\dot{\phi}_i \right] \\
m_1 \ddot{z}_1 - \frac{k_1}{n^2} \sum_{i=1}^6 (2nL\sin\theta - |\Psi_i|) \frac{\partial |\Psi_i|}{\partial z_1} - \frac{k_2}{n^2} \sum_{i=1}^6 \left(1 - \frac{2nL\cos\theta}{\sqrt{4n^2L^2 - |\Psi_i|^2}} \right) |\Psi_i| \\
\left| \frac{\partial |\Psi_i|}{\partial z_1} \right| = \sum_{i=1}^6 \left[-2(3n+1)c\dot{\phi}_i \right] \\
m_2 \ddot{z}_2 - \frac{k_1}{n^2} \sum_{i=1}^6 (2nL\sin\theta - |\Psi_i|) \frac{\partial |\Psi_i|}{\partial z_2} - \frac{k_2}{n^2} \sum_{i=1}^6 \left(1 - \frac{2nL\cos\theta}{\sqrt{4n^2L^2 - |\Psi_i|^2}} \right) |\Psi_i| \\
\left| \frac{\partial |\Psi_i|}{\partial z_2} \right| = \sum_{i=1}^6 \left[-2(3n+1)c\dot{\phi}_i \right]
\end{aligned}$$

As we can see from these equations, we can see that all variables are coupled with each other, which it is difficult for us to solve. To analyze the dynamic responses in all directions, it is assumed that the variables in the other DOFs are zero when the targeted variable is investigated for simplicity of discussions. For instance, when \dot{x} is the objective variable, the variable \dot{y} and \dot{z} are equal to zero. Due to the structural symmetry of the Stewart platform, the same vibration isolation performance can be obtained in the x and y directions, which can be confirmed later. Therefore, attentions will be paid to the analyses of the vibration isolation performance of the XSSIP system in the x and z directions in the following parts.

3.1. Approximation of Taylor series expansion

In the above dynamic equations, nonlinear functions in terms of displacement and the structural parameters are rather complicated, so the Taylor series expansion is always made use of to approximate the nonlinear functions. All coefficients are constant corresponding to the structural parameters such as the rod length, the spring stiffness, the layer number of the X-shape structure and so on. To validate the accuracy of Taylor expansions, some comparisons are presented in Figs. 7 and 8. In this calculation, all structural parameters are chosen as follows: $m_1 = 4 \text{ kg}$, $m_2 = 200 \text{ kg}$, $c_1 = 0.2 \text{ N}\cdot\text{s}/\text{m}$, $c_3 = 0.2 \text{ N}\cdot\text{s}/\text{m}$, $c = 0.1 \text{ N}\cdot\text{s}/\text{m}$, $L = 0.1 \text{ m}$, $\theta = \pi/3 \text{ rad}$, $n = 3$, $k_1 = 0 \text{ N/m}$, $k_2 = 1000 \text{ N/m}$, $r_1 = 0.30 \text{ m}$, $r_2 = 0.26 \text{ m}$.

Next we apply the 3rd-order Taylor series expansion to approximate the original nonlinear functions. Therefore, the dynamic equations of motions can be written by Taylor series expansion

$$\begin{aligned}
m_1 \ddot{x}_1 - [a_{11}(x_2 - x_1) + a_{12}(x_2 - x_1)^2 + a_{13}(x_2 - x_1)^3] - c_1(\dot{x}_2 - \dot{x}_1) \\
- 2(3n+1)c[a_{20} + a_{21}(x_2 - x_1) + a_{22}(x_2 - x_1)^2 + a_{23}(x_2 - x_1)^3] \\
(\dot{x}_2 - \dot{x}_1) = 0 \\
m_2 \ddot{x}_2 + [a_{11}(x_2 - x_1) + a_{12}(x_2 - x_1)^2 + a_{13}(x_2 - x_1)^3] + c_1(\dot{x}_2 - \dot{x}_1) \\
+ 2(3n+1)c[a_{20} + a_{21}(x_2 - x_1) + a_{22}(x_2 - x_1)^2 + a_{23}(x_2 - x_1)^3] \\
(\dot{x}_2 - \dot{x}_1) = 0 \\
m_1 \ddot{z}_1 - [b_{10} + b_{11}(z_2 - z_1) + b_{12}(z_2 - z_1)^2 + b_{13}(z_2 - z_1)^3] - c_3(\dot{z}_2 - \dot{z}_1) \\
- 2(3n+1)c[b_{20} + b_{21}(z_2 - z_1) + b_{22}(z_2 - z_1)^2 + b_{23}(z_2 - z_1)^3] \\
(\dot{z}_2 - \dot{z}_1) = 0 \\
m_2 \ddot{z}_2 + [b_{10} + b_{11}(z_2 - z_1) + b_{12}(z_2 - z_1)^2 + b_{13}(z_2 - z_1)^3] + c_3(\dot{z}_2 - \dot{z}_1) \\
+ 2(3n+1)c[b_{20} + b_{21}(z_2 - z_1) + b_{22}(z_2 - z_1)^2 + b_{23}(z_2 - z_1)^3] \\
(\dot{z}_2 - \dot{z}_1) = 0
\end{aligned}$$

where all coefficients of the 3rd-order Taylor expansions are directly computed by Mathematica and the concrete expressions are not listed because of their complexity.

Let

$$\begin{aligned}
\tilde{f}_i &= a_{i0} + a_{i1}(x_2 - x_1) + a_{i2}(x_2 - x_1)^2 + a_{i3}(x_2 - x_1)^3, \\
\tilde{g}_i &= b_{i0} + b_{i1}(z_2 - z_1) + b_{i2}(z_2 - z_1)^2 + b_{i3}(z_2 - z_1)^3. \quad (i = 1, 2)
\end{aligned}$$

From Figs. 7 and 8, the 3rd-order Taylor expansions are in a good agreement with the original terms in either x or z direction, which means that the 3rd-order Taylor series expansion is enough for the accuracy of further study.

In the next two sections, we investigate the vibration isolation performance of the XSSIP system for the two cases: under periodic external excitation and under the impulsive force, which are studied in detail later. As mentioned earlier, due to the structural symmetry, the vibration isolation performance in the x direction is completely as same as that in the y direction, which is neglected in the following investigation.

4. Vibration isolation performance of the XSSIP system under periodic external excitation

In this section we investigate the vibration isolation performance of the XSSIP system in the case that the system is subjected to the periodic external excitation. The displacement transmissibility is defined as the ratio between vibration amplitude of the satellite platform and that of the capture mechanism in each direction, that is, $T_d = A_{m2}/A_{m1}$. The displacement transmissibilities of the XSSIP system in three directions are shown in Fig. 9. As we can see from this figure, the XSSIP system can realize the better vibration isolation performance in all directions. It is noted that the displacement transmissibility of the XSSIP system agrees well in the x and y directions, which is in good agreement with the description in the preceding section. Therefore, we study the vibration isolation performances of the XSSIP system in the x and z directions ignoring the case that in the y direction.

4.1. The vibration response in space mission

First the vibration isolation responses of the XSSIP system subjected to the periodic external excitation in the x and z directions will be studied. The amplitude frequency response curves in two directions are shown in Fig. 10. It is noted that the ultra frequency range is not plotted considering the fact that $\omega \rightarrow 0$ results in a dramatically increasing amplitude. The response will become extremely weak when the excitation frequency is much larger than the resonant frequency. Therefore, more attentions will be paid to the low frequency range. In the x direction, the amplitude of A_{x2} in blue line is far smaller than that of A_{x1} in red line in Fig. 10 (a). In the z direction, for the low frequency range $\omega < 3.8 \text{ rad/s}$, the amplitude of A_{z2} in blue line is relatively larger than that of A_{z1} in red line in Fig. 10 (b). And in the frequency range

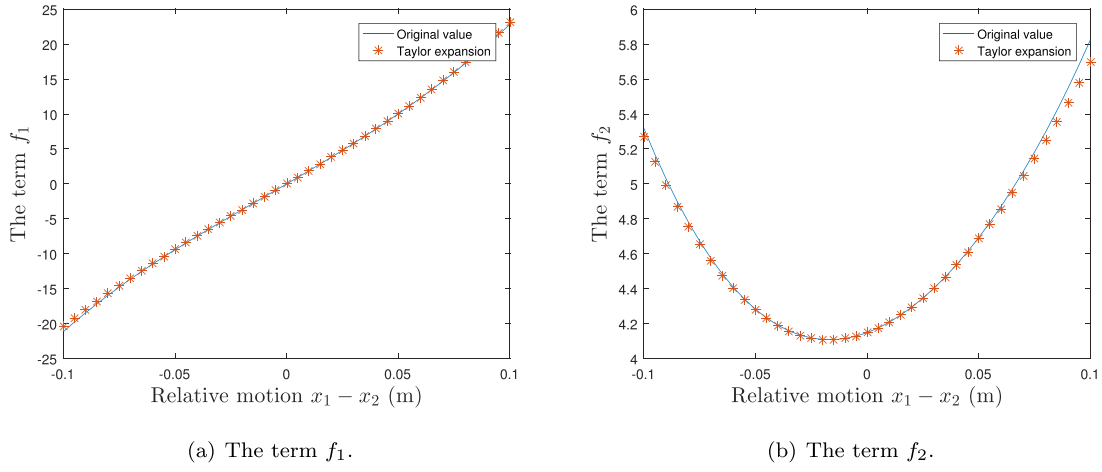


Fig. 7. Comparisons between the original terms and the 3rd-order Taylor-expansions for f_1 and f_2 in the x direction.

$\omega > 3.8 \text{ rad/s}$, the amplitude of A_{z2} is markedly much smaller than that of A_{z1} . In the practical space mission, the excitation frequency is mainly distributed in from a few to a few hundreds hertz, which can be regarded as the high frequency excitation in the present system. Therefore, no matter in which direction the XSSIP system is, the vibration amplitude of the satellite platform is greatly reduced in comparison with that of the capture mechanism subjected to the periodic external excitations. It is very efficient for suppressing the post-capture vibrations in this case carrying out the space mission.

4.2. Comparison with the SMD-based Stewart isolation platform system

In this part, we compare the present XSSIP system with the Stewart platform system, whose “legs” are substituted by the traditional SMD isolator, referred to as SMD-based Stewart isolation platform (SMD-SIP) system, to demonstrate the superiority of the XSSIP system in suppressing post-capture vibrations subjected to the periodic external excitation. The displacement transmissibilities of the XSSIP system and the SMD-SIP isolator are shown in Fig. 11, where the same spring stiffness ($k = 1000 \text{ N/m}$) is employed and the horizontal spring in the XSSIP system is neglected for relatively fair comparison. In Fig. 11, the red curve stands for the vibration response of the XSSIP system and the blue one represents that of the SMD-SIP system. It is evident that the vibration isolation performance of the XSSIP system is markedly superior to that of the latter one and significant differences between them

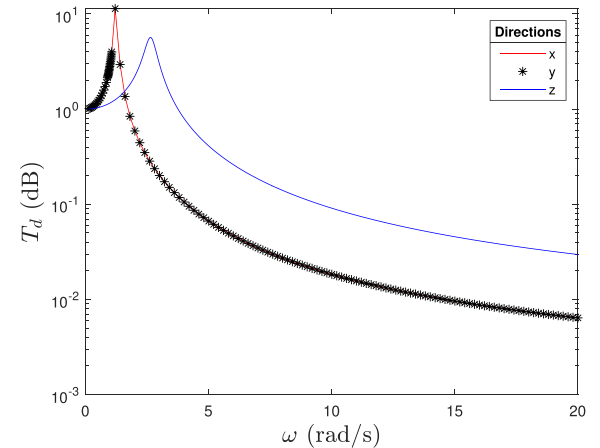


Fig. 9. Displacement transmissibilities in three directions.

can be clearly observed. First, the resonant frequency of the XSSIP system is much smaller than that of the SMD-SIP isolator. Meanwhile, the nonlinear damping characteristic of the XSSIP system due to the existence of the X-shape structure contributes to the suppression of the amplitude of the peak without increasing the slope of the

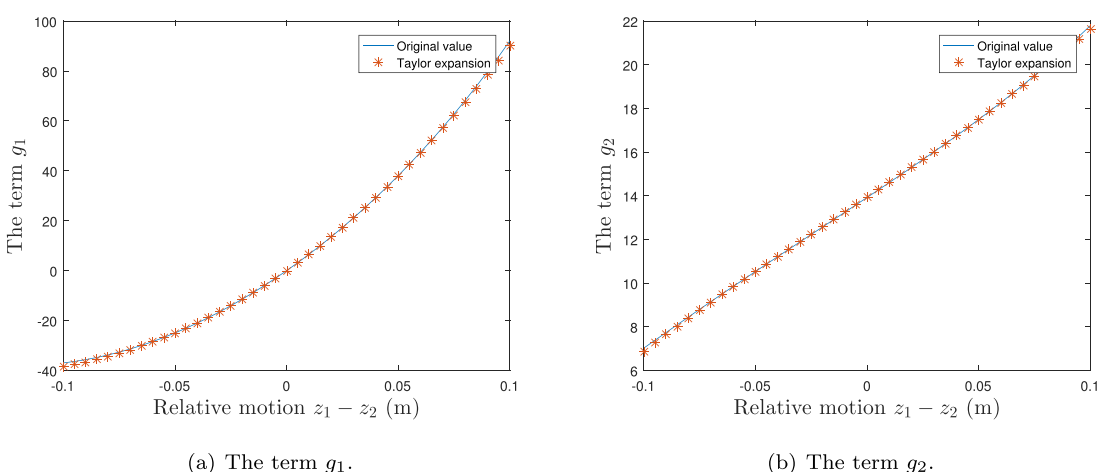


Fig. 8. Comparisons between the original terms and the 3rd-order Taylor-expansions for g_1 and g_2 in the z direction.

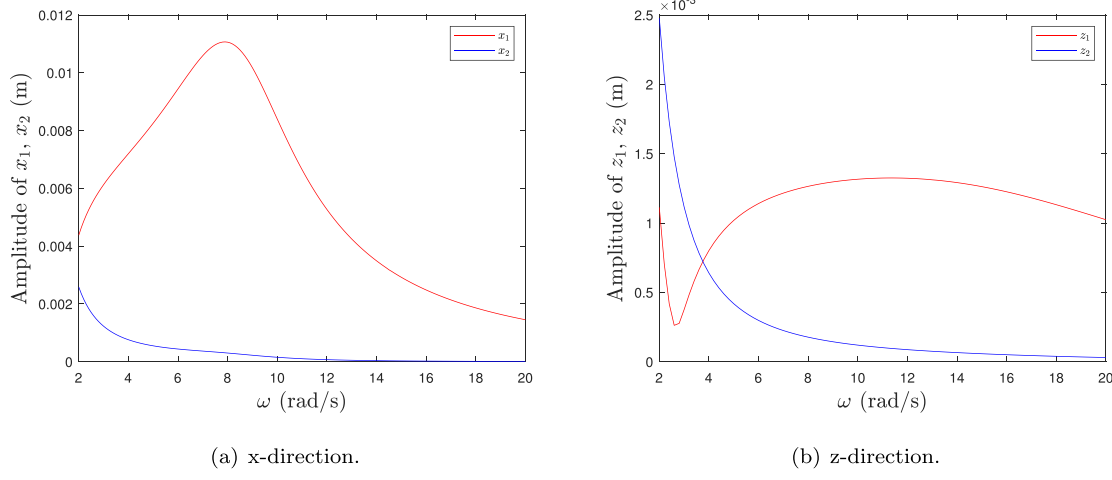


Fig. 10. Amplitude frequency response curve subjected to the periodic external excitation.

transmissibility as seen in the SMD-SIP system. In addition, the displacement transmissibility of the XSSIP system is much lower than that of the latter one at high frequency region. The vibration isolation responses of two systems in the x direction are similar to those in the z direction. These demonstrate the superiority of the X-shape structure to the traditional SMD isolator in the Stewart platform isolation system explicitly.

4.3. Influence of different parameters

The structural parameters of the XSSIP system can be designed randomly for different vibration isolation performance. In this work, the key structural parameters include the rod length L , the spring stiffness k , the masses m_1 and m_2 , the layer number of the X-shape structure n , the radius r_1 and r_2 of the Stewart platform and the assembly angle of connecting rods θ . The resonant frequency and maximum displacement transmissibility are employed as two indicators to demonstrate the influences on the vibration isolation performance with different structural parameters. In the following part, the structural parameters are chosen as follows: $m_1 = 4 \text{ kg}$, $m_2 = 200 \text{ kg}$, $c_1 = 0.2 \text{ N}\cdot\text{s}/\text{m}$, $c_3 = 0.2 \text{ N}\cdot\text{s}/\text{m}$, $c = 0.1 \text{ N}\cdot\text{s}/\text{m}$, $L = 0.1 \text{ m}$, $\theta = \pi/3 \text{ rad}$, $n = 3$, $k_1 = 0 \text{ N/m}$, $k_2 = 1000 \text{ N/m}$, $r_1 = 0.30 \text{ m}$, $r_2 = 0.26 \text{ m}$. When one of the above parameters is studied, it is only chosen as different value and the other parameters are constant.

4.3.1. Effect of the spring stiffness

As we described in the previous section, there exist two kinds of springs in the XSSIP system: the horizontal and vertical springs. Here, we define the stiffness of two springs as equal to investigate the influence of the spring stiffness on the vibration isolation performance. Fig. 12 shows the effects of the spring stiffness on the displacement transmissibility of system. It can be seen that the curves in Fig. 12 (a) and (b) are consistent on the whole. The vibration isolation performances of the XSSIP system are obviously influenced by the spring stiffness. Decreasing the spring stiffness can reduce the peak value of displacement transmissibility and the natural frequency, which is desired on the vibration isolation of system. The XSSIP system has even lower resonant frequency range, which is thus helpful for low frequency vibration isolation with a smaller k . Moreover, the vibration isolation performance at the higher frequency range can be improved obviously with decreasing the spring stiffness k . Therefore, in practical applications, choosing a smaller spring stiffness is beneficial to achieve the better vibration isolation performance of the present system.

4.3.2. Effect of the rod length

The displacement transmissibilities for different length of the supporting rod are shown in Fig. 13. Different from the previous cases, influences of the rod length on the vibration isolation performance of the XSSIP system are distinct in the x and z directions. In the x direction, increasing the rod length L can reduce the natural frequency but

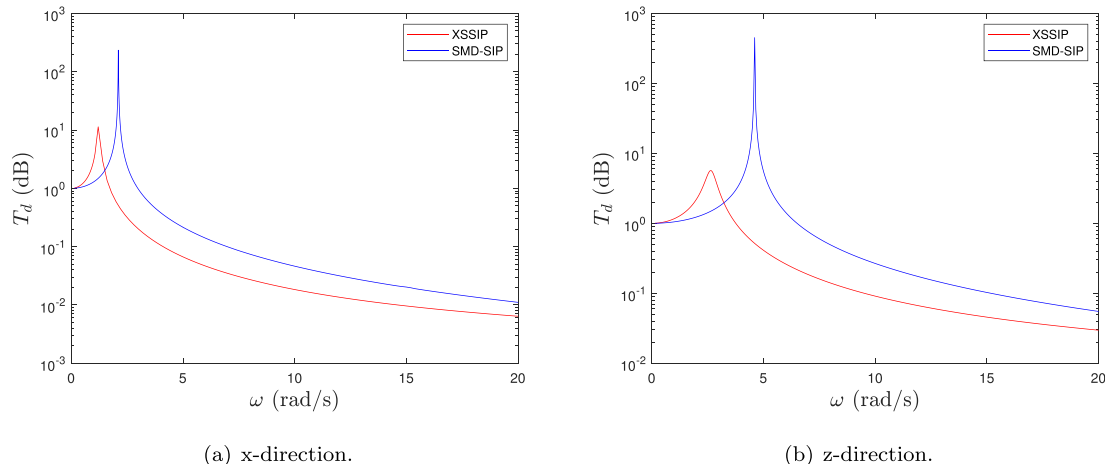
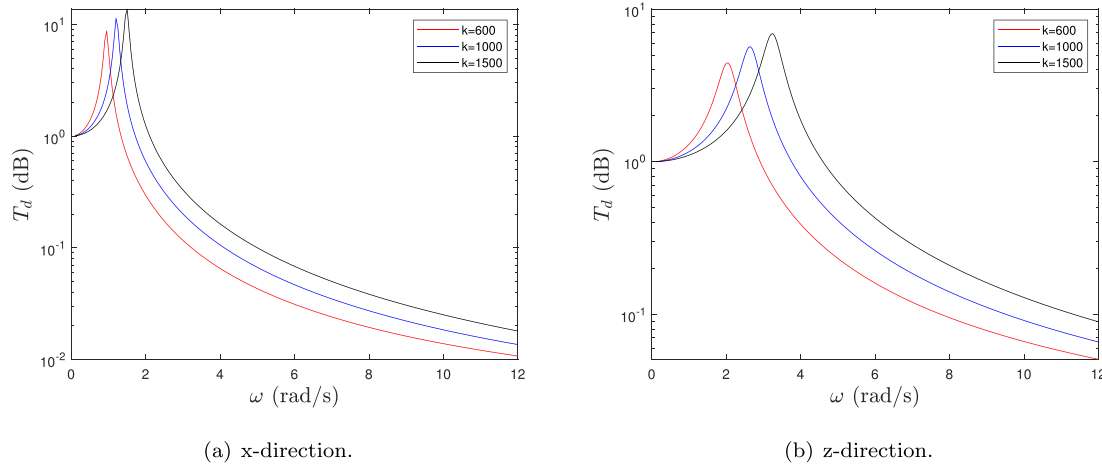


Fig. 11. Comparisons between the XSSIP system and the traditional SMD-SIP isolator subjected to the periodic external excitation.

Fig. 12. Displacement transmissibilities with different spring stiffness k .

enlarge the peak amplitude on the displacement transmissibility slightly. Moreover, a larger L leads to the better vibration isolation performance over the high frequency range. In a word, a longer rod is helpful to isolate the vibrations in the x direction. However, it is the other way around in the z direction. The smaller the rod length is, the better vibration isolation performance the XSSIP system has. A shorter supporting rod is required to achieve the smaller natural frequency and the lower displacement transmissibility on the entire frequency range. Therefore, the compromise between the two directions should be considered in terms of the supporting rod length.

4.3.3. Effect of the masses

The influences of the masses with regard to m_1 and m_2 on the vibration isolation performance of the XSSIP system are depicted in Figs. 14 and 15, respectively. For m_1 , it is obvious that changing the mass m_1 has no effect on the displacement transmissibility of system, that is, the vibration isolation performance is almost independent on m_1 . On the contrary, the curve about the displacement transmissibility for m_2 is obviously different. It can be seen clearly that increasing the mass m_2 can reduce the resonant frequency and improve the vibration isolation performance over the relative higher frequency region, which enlarges the peak amplitude on the natural frequency slightly. Thus, a larger m_2 corresponds to a smaller resonant frequency and a better vibration isolation performance in the high frequency range, which is consistent with the fact that the heavier m_2 makes the whole system

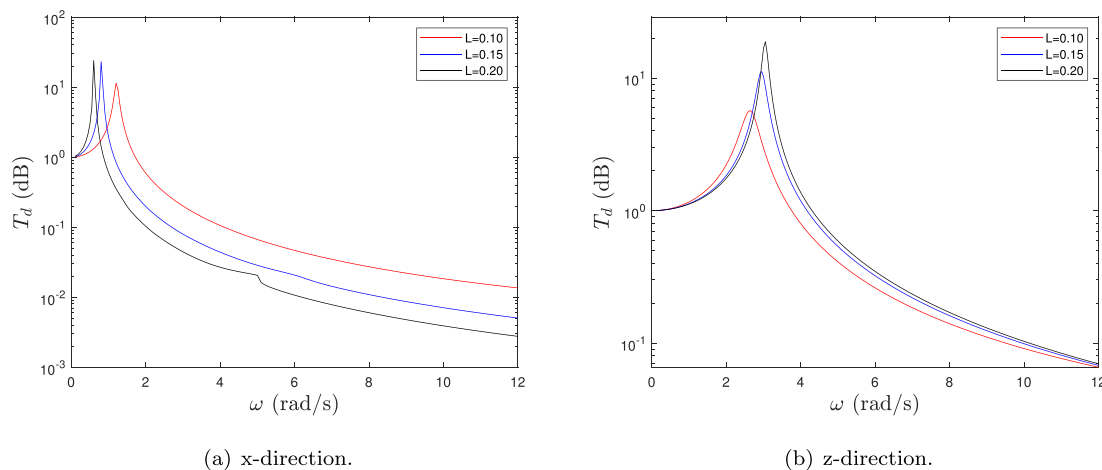
more stable. In summary, it is desirable to use the heavier satellite platform irrespective of the capture mechanism m_1 .

4.3.4. Effect of the number of layers

The effects of the layer number n of the X-shape structure on the vibration isolation performance are displayed in Fig. 16. It shows that both the resonant frequency and the displacement transmissibility over the high frequency region are decreased with the increasing layer number of the X-shape structure. It is obvious that the natural frequency of the XSSIP system is reduced by using more layers in each leg, which is helpful to vibration suppression. A larger n leads to the better vibration isolation performance of the present system, but more layer X-shape structure can increase the complexity of the whole system, which results in the issue with regard to stability.

4.3.5. Effect of the radius of the Stewart platform

Figs. 17 and 18 show the displacement transmissibilities of the XSSIP system with different radius of two platforms, respectively. In the x direction, the curves in Fig. 17 (a) and 18 (a) agree with each other basically. A relatively smaller radius r_1 can obtain the smaller resonant frequency and the lower displacement transmissibility over the high frequency region, but increase the response amplitude in the resonant peak. However, the case is opposite in the z direction. It can be seen from Fig. 17 (b) and 18 (b) that when the radius of the left or right platform becomes larger, the resonant frequency in the z direction is

Fig. 13. Displacement transmissibilities with different length of supporting rod L .

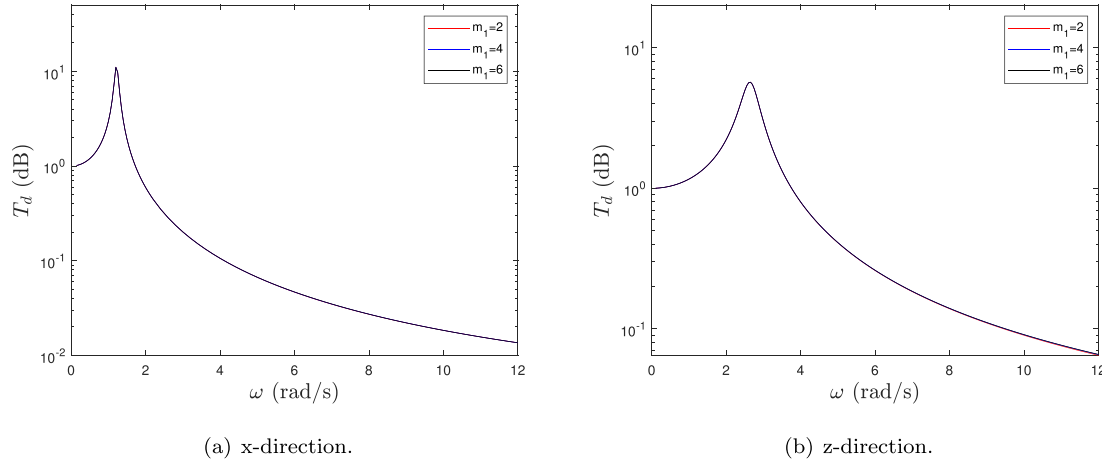


Fig. 14. Displacement transmissibilities with different mass of the capture mechanism m_1 .

smaller and the displacement transmissibility is lower at the high frequency region, while the tendency of x direction is opposite and the vibration isolation performance is worse. No matter what the radius of the Stewart platform is, the peak value in the resonant frequency range is almost same, which has little effect on the vibration isolation performance of the XSSIP system. In comprehensive considerations of both directions, a larger r_1 and a smaller r_2 are desired in practical applications to achieve the better vibration isolation performance of the present system. The radius of the Stewart platform should be balanced according to the requirements of practical engineering, which is a critical parameter to reduce the vibration transmissibility and improve the vibration isolation performance of the XSSIP system.

4.3.6. Effect of the assembly angle of connecting rods

The other structural parameters are set to the same as before, while the rod assembly angle θ is considered as $\pi/6$, $\pi/5$, $\pi/4$. The displacement transmissibilities T_d of the XSSIP system are revealed in Fig. 19. It can be seen clearly that the vibration isolation response in the x direction differs from that in the z direction at the higher frequency region and the trend of the curves is similar around the resonant frequency. In around the resonant frequency region, increasing the assembly angle θ can lead to the increase of the natural frequency, which is undesired in practical engineering. A smaller θ can reduce the displacement transmissibility at the higher frequency region in the z direction. However, the tendency of the displacement transmissibility

curve is different at various higher frequency region in the x direction. The change in the higher frequency range is relatively mild. Therefore, a smaller assembly angle of the connecting rods is beneficial to improve the vibration isolation performance of the XSSIP system in either x or z direction.

5. Vibration isolation performance of the XSSIP system under an impulsive external force

In this section, vibration isolation performance of the XSSIP system subjected to an impulsive external force will be investigated detailedly. It is of great importance to capture a target successfully in the on-orbit missions. Due to the existence of the collisions between the capture mechanism and the target, it is significant to suppress the post-capture vibrations efficiently. Because the impulsive forces act on the XSSIP system during a negligibly small period of time, the generalized momenta are equal to and thus can be referred to as generalized impulses. Therefore, the effect of the impulses acting the system can be converted into the system's initial states. For brevity, the impulsive force is replaced by imposing an initial velocity into the capture mechanism. Here, the system parameters are as follows: $m_1 = 4 \text{ kg}$, $m_2 = 200 \text{ kg}$, $c_1 = 0.2 \text{ N}\cdot\text{s}/\text{m}$, $c_3 = 0.2 \text{ N}\cdot\text{s}/\text{m}$, $c = 0.1 \text{ N}\cdot\text{s}/\text{m}$, $L = 0.1 \text{ m}$, $\theta = \pi/3 \text{ rad}$, $n = 3$, $k_1 = 0 \text{ N/m}$, $k_2 = 1000 \text{ N/m}$, $r_1 = 0.30 \text{ m}$, $r_2 = 0.26 \text{ m}$, $I = 0.6 \text{ kg}\cdot\text{m/s}$ unless otherwise mentioned.

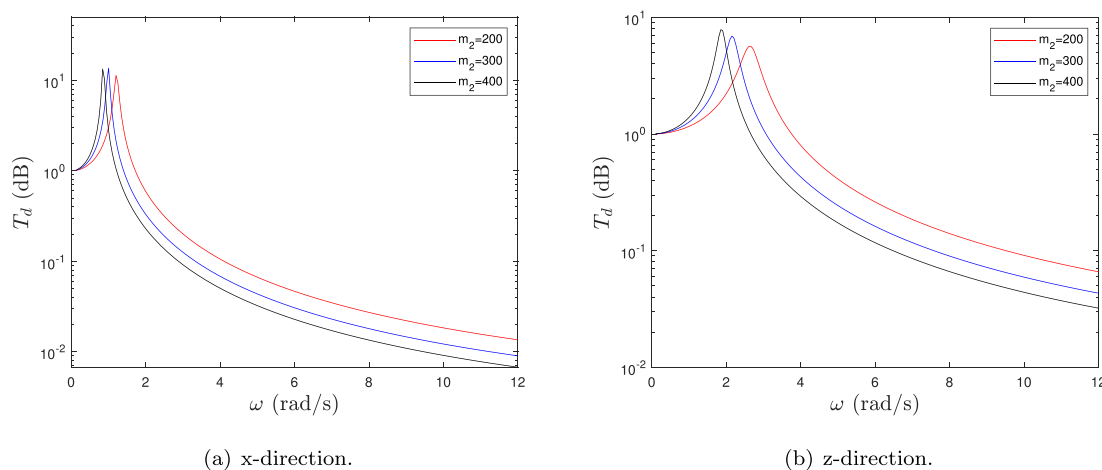


Fig. 15. Displacement transmissibilities with different mass of the satellite platform m_2 .

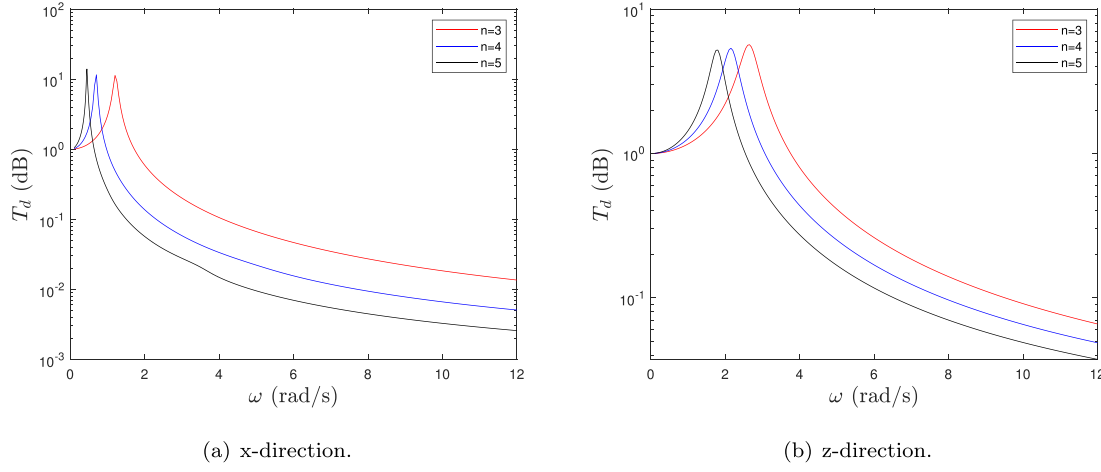


Fig. 16. Displacement transmissibilities with different layer number of the X-shape structure n .

5.1. The vibration response in space mission

As we discussed before, the vibration isolation performances in the x and z directions are studied detailedly, neglecting the y-direction due to the structural symmetry of platform. The vibration isolation performances of the XSSIP system in the x and z directions are shown in Figs. 20 and 22, where the red curves represent the responses of the XSSIP system. First, we observe the velocity histories of the XSSIP system subjected to an impulse in Figs. 20 and 22. Take the behaviors of the XSSIP system in the x direction for instance. As the figure shows, the curves of x_1 and x_2 vibrate at the initial stage for few seconds and approach to an oblique line eventually. It implies the case that the motions include the simultaneous vibrational and translational components. With the existence of the nonlinear damping, the vibrational part disappears and the tendency of the curve is along with an oblique line finally. The trends of \dot{x}_1 and \dot{x}_2 over time are displayed in Fig. 20 (c) and (d), respectively. From this figure, we can find that the initial velocity of x_1 is 0.15 m/s with the influence of the impulsive force and that of x_2 starts with zero. Both of them vibrate for a short period of time and become constant after about 3 s. It is noted that the velocity of x_2 is obviously smaller than that of x_1 , which demonstrates the superiority of suppressing the post-capture vibrations subjected to an impulsive force. In addition, the whole system does not stop and drifts at a speed of 0.29 cm/s due to the existence of translational components. To study the vibration isolation performance better, the vibrational component

holds on and the translational one is eliminated in this direction. The responses of the two masses are plotted in Fig. 21. This figure shows that the two masses stop and become stable in about 3 s. The maximums of x_1 and x_2 are 1.1×10^{-2} m and 2.2×10^{-4} m, which confirms the vibration isolation performance of the present system. Next, the velocity and acceleration histories of two masses are shown in Fig. 21 (c)–(f). The maximum velocities of two masses are 6.1×10^{-2} m/s and 4.2×10^{-3} m/s, respectively. By comparing the maximum velocities of two masses, we can find that the vibrations are reduced remarkably through the suppression of the XSSIP system. Acceleration is always referred to as the important index to measure the vibration isolation performances of system. The maximums of \ddot{x}_1 and \ddot{x}_2 are 1.058m/s^2 and 0.021m/s^2 , respectively. The acceleration of the satellite platform \ddot{x}_2 is much smaller than that of the capture mechanism \ddot{x}_1 obviously, which is desired in the capture mission. In addition, responses of the XSSIP system in the z direction are similar with that in the x direction, so we do not elaborate it. All in all, the vibrations of the satellite platform are reduced markedly subjected to an impulsive external force arisen in space mission.

5.2. Comparison with the SMD-based Stewart isolation platform system

In order to demonstrate the superiority of the XSSIP system better, we compare it with the SMD-based Stewart isolation platform system in suppressing the post-capture vibrations subjected to an impulsive force.

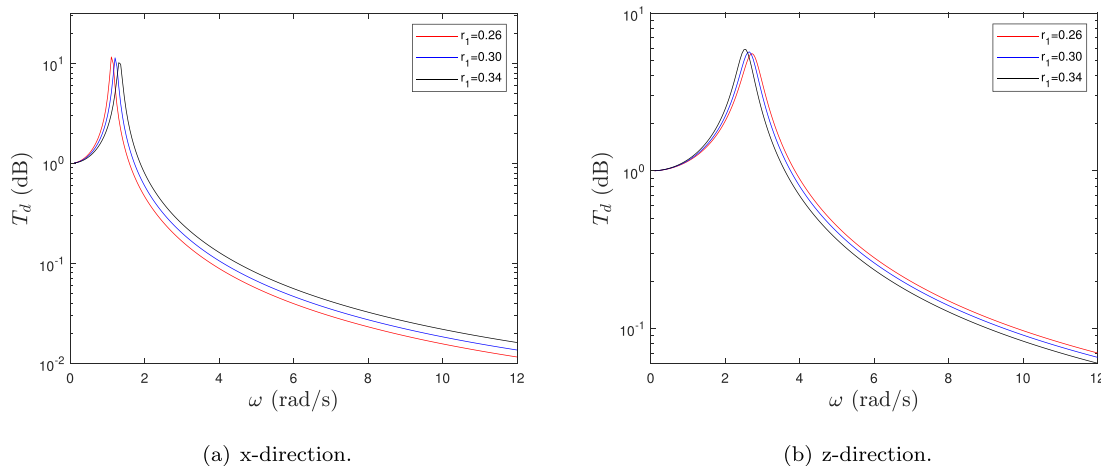


Fig. 17. Displacement transmissibilities with different radius of right platform r_1 .

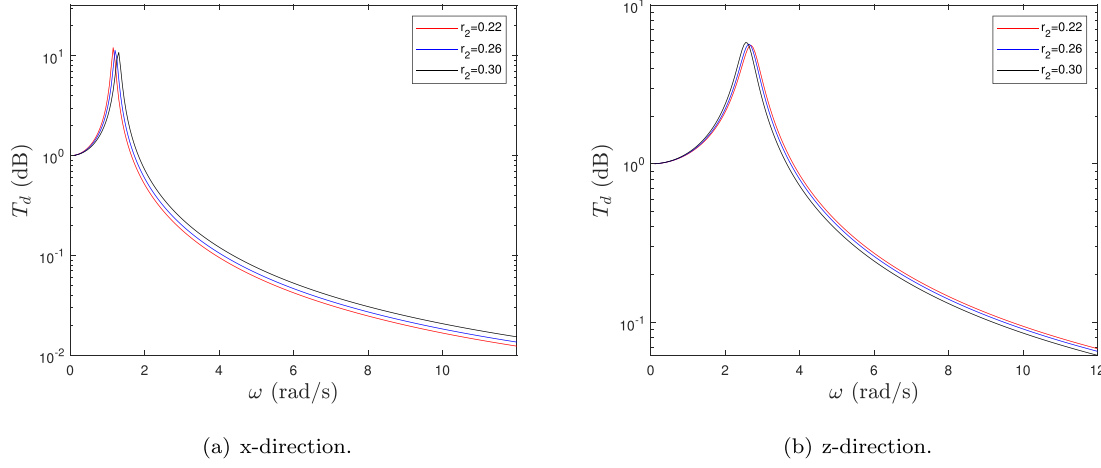


Fig. 18. Displacement transmissibilities with different radius of left platform r_2 .

The vibration performances of two kinds of vibration isolation system are depicted in Figs. 20–23. It is clearly seen that responses of the XSSIP system and the SMD-SIP system are similar basically, no matter which direction the systems are in. Take the responses of the XSSIP and SMD-SIP systems in the x direction for instance. For Fig. 21 (a)–(b), although the maximum displacement of the XSSIP system is larger than that of the SMD-SIP system, the vibrations of the former system stop quickly and meanwhile the vibrations of the latter one last for a long time with a small drop. For the velocity and acceleration terms, the vibration amplitude of the XSSIP system is obviously smaller than that of the SMD-SIP system, which is satisfactory. In addition, the SMD-SIP system can generate the high frequency vibrations when subjected to an impulsive force acting on the capture mechanism, which can do damage to the precise payloads mounted on the satellite platform. At the same time, the vibrations can be disappeared quickly under the effect of nonlinear damping and stiffness of the XSSIP system. The same conclusions can be drawn in the z direction. In summary, the vibration isolation performance of the XSSIP system is much better than that of the SMD-SIP isolator in suppressing the post-capture vibrations subjected to an impulsive force.

5.3. Effect of the impulse magnitude

In this part, the dynamic responses when subjected to the different impulse magnitude are investigated in the x and z direction. The

displacement, velocity and acceleration histories evolving with time in terms of two masses are shown in Fig. 24. For the case in the x direction, the maximum vibration amplitudes of x_1 are 0.75×10^{-2} m, 1.11×10^{-2} m, 1.48×10^{-2} m and that of x_2 are 1.50×10^{-4} m, 2.24×10^{-4} m, 2.96×10^{-4} m with respect to $I = 0.4, 0.6, 0.8$ kg·m/s, respectively. We can find that the amplitudes for each case are proportional to the impulse force and the maximum of x_2 is far smaller than that of x_1 , which demonstrates the good vibration isolation performance. As the figure shows, the maximum of \dot{x}_1 takes place in the initial time with the existence of an impulsive force and the velocity \dot{x}_2 starts with zero through the vibration translation of the X-shape structure. As we discussed previously, the drift motions exist and the drifting speeds of \dot{x}_1 and \dot{x}_2 are identical exactly for different amplitude impulses. The capture mechanism and the satellite platform are synchronous and translate at the same speed finally. The accelerations of m_1 and m_2 are shown in Fig. 24 and the maximums are 0.70 m/s², 1.06 m/s², 1.42 m/s² for \ddot{x}_1 and 1.40×10^{-2} m/s², 2.12×10^{-2} m/s², 2.84×10^{-2} m/s² for \ddot{x}_2 , respectively. The larger impulsive force leads to the larger acceleration for m_1 and m_2 . For the case in the z direction, the curves are similar with that in the x direction basically. The maximum vibration amplitudes of z_1 are 2.50×10^{-3} m, 3.80×10^{-3} m, 5.09×10^{-3} m and those of z_2 are 4.99×10^{-5} m, 7.51×10^{-5} m, 1.01×10^{-4} m with respect to $I = 0.4, 0.6, 0.8$ kg·m/s, respectively. Similarly, the maximum velocity \dot{z}_1 emerges in the initial time due to the impulsive force and that of \dot{z}_2 begins with zero. Different from the case that in the x direction, the

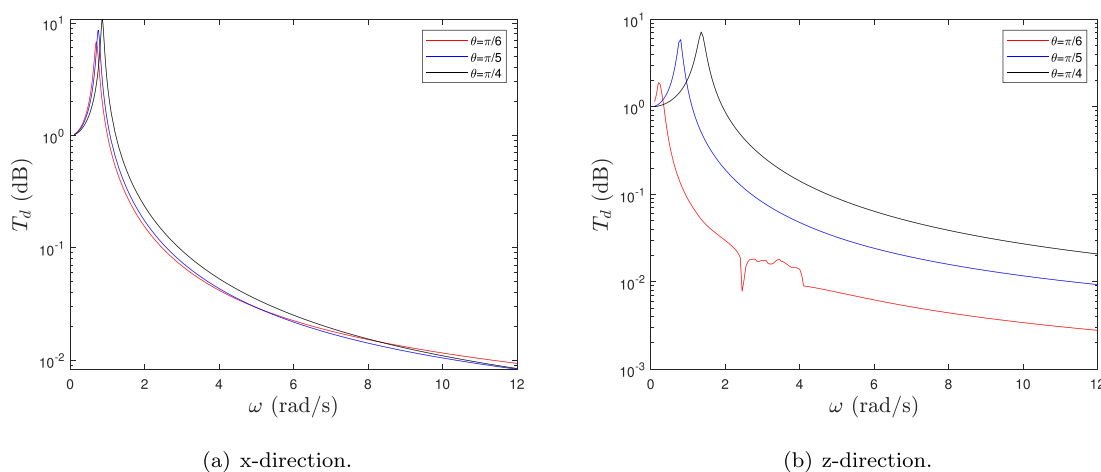


Fig. 19. Displacement transmissibilities with different assembly angle of connecting rods θ .

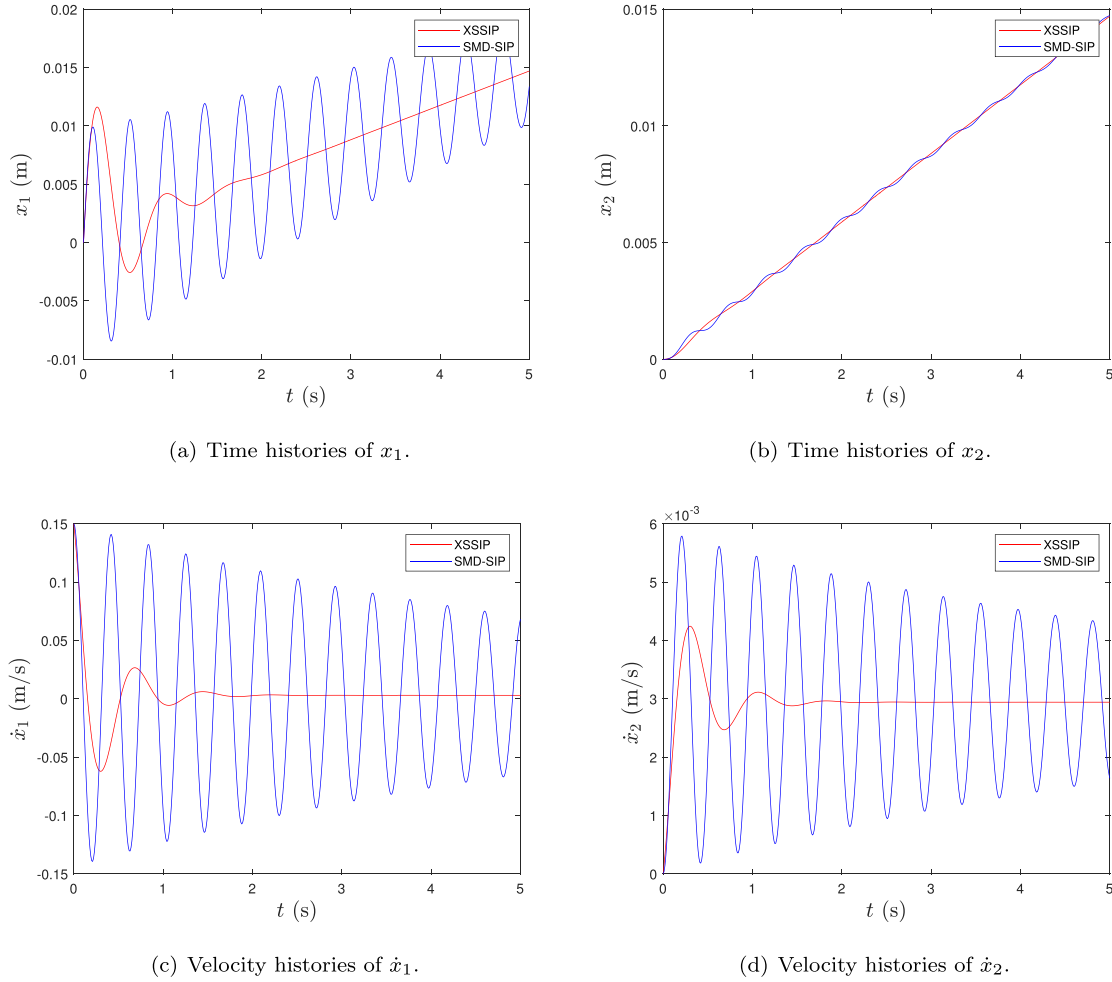


Fig. 20. Vibration isolation performance in the x direction subjected to an impulse $I = 0.6 \text{ kg}\cdot\text{m/s}$.

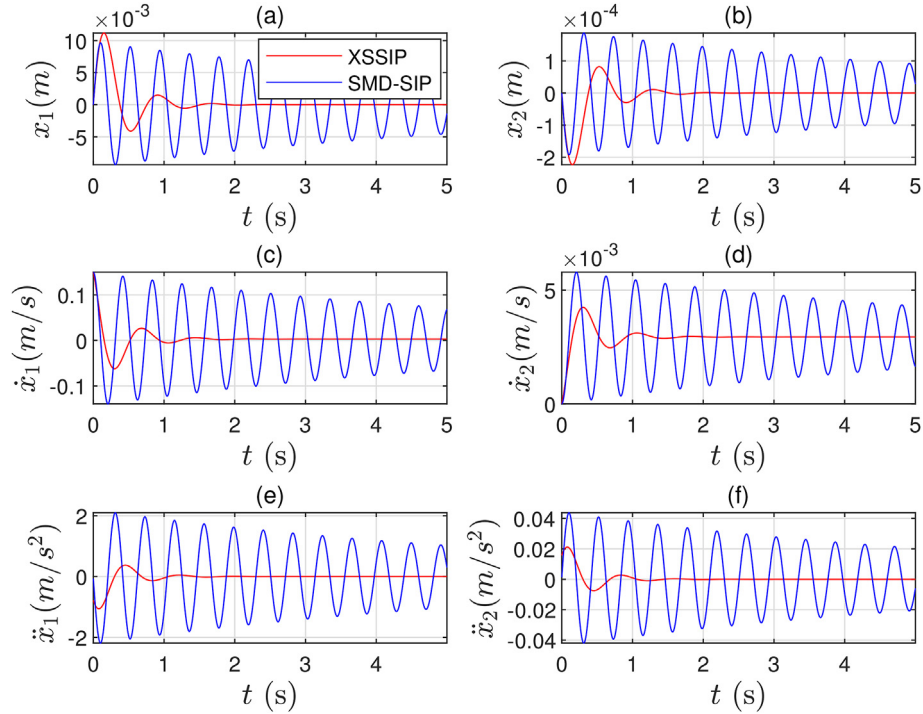


Fig. 21. Vibration isolation performance in the x direction subjected to an impulse $I = 0.6 \text{ kg}\cdot\text{m/s}$ without drift motion.

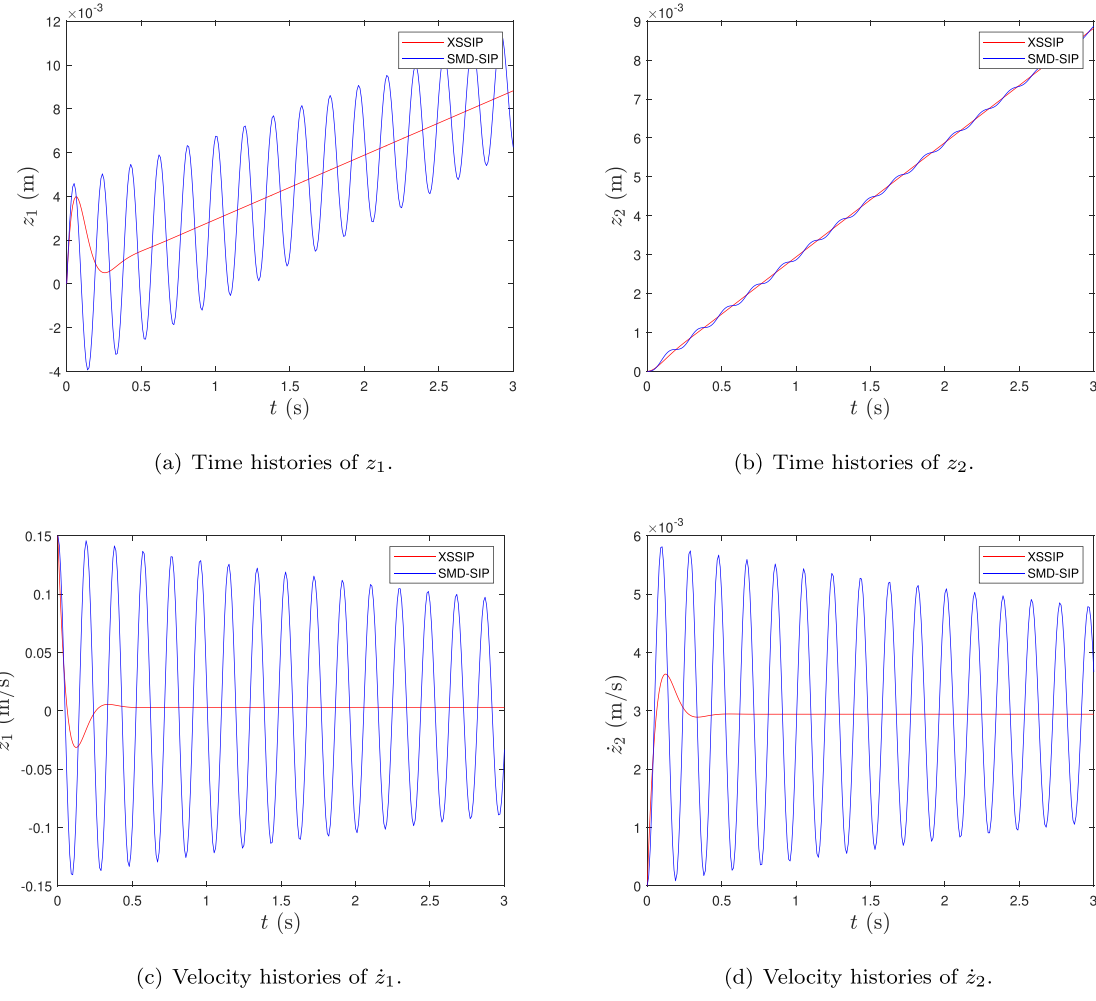


Fig. 22. Vibration isolation performance in the z direction subjected to an impulse $I = 0.6 \text{ kg}\cdot\text{m/s}$.

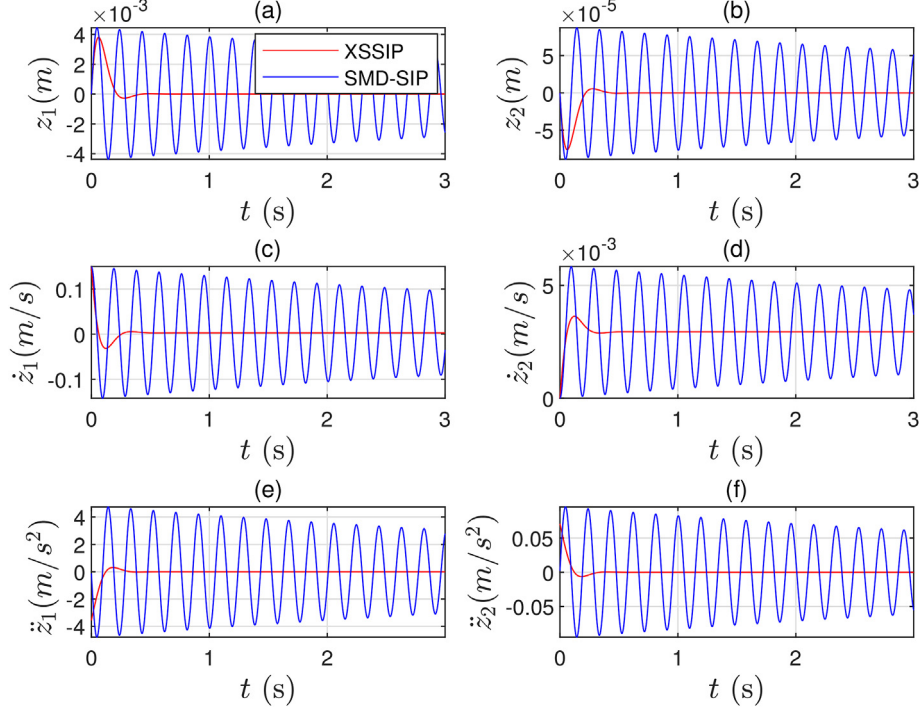


Fig. 23. Vibration isolation performance in the z direction subjected to an impulse $I = 0.6 \text{ kg}\cdot\text{m/s}$ without drift motion.

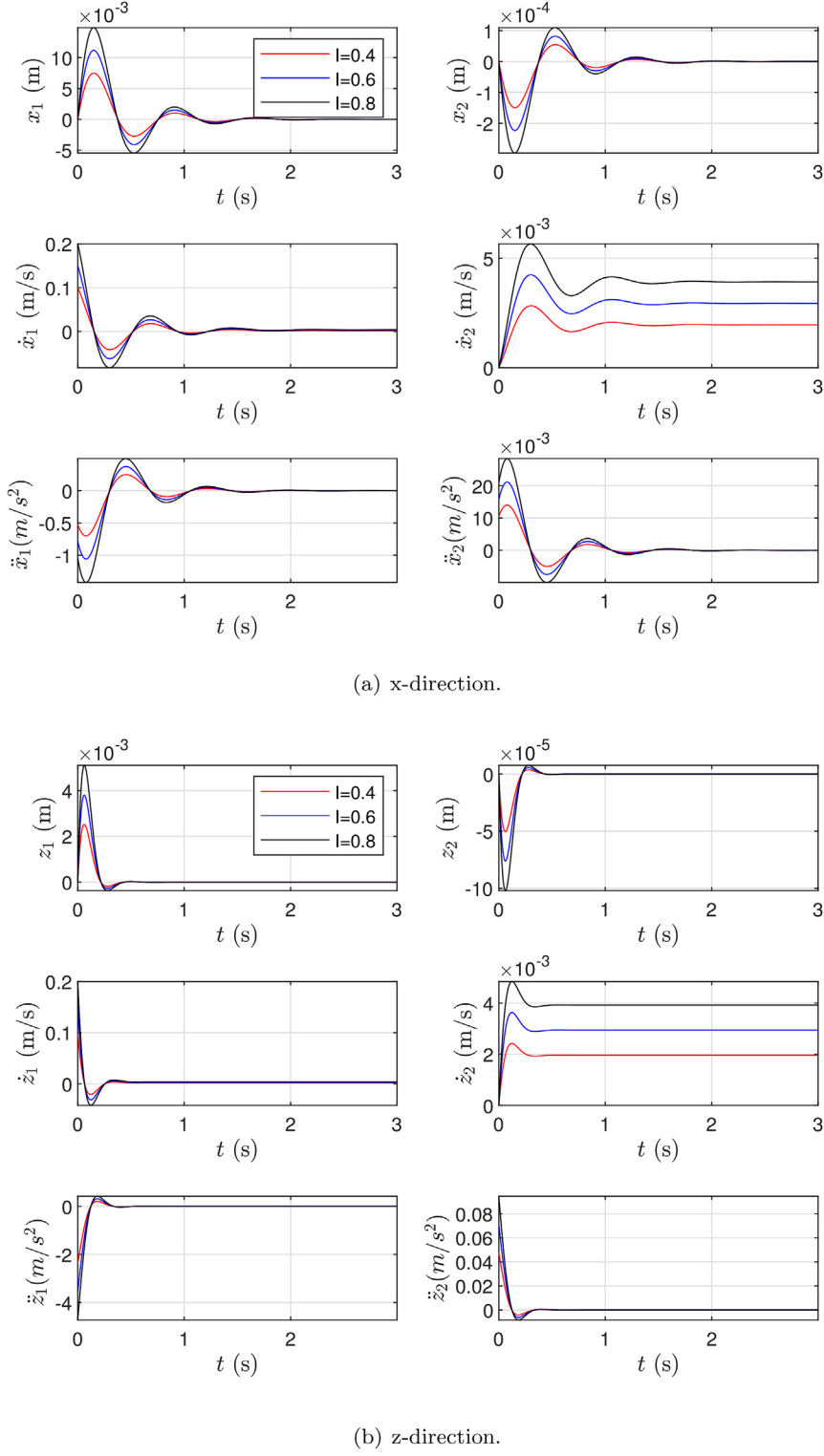


Fig. 24. Comparisons with different impulse magnitude.

maximum acceleration appears in the beginning and decreases evolving with time. Compared with the dynamic responses in the x direction, the amplitude in the z direction is obviously smaller than that in the x direction when subjected to the same impulsive force. Therefore, it takes less time in the z direction than that in the x direction to suppress the vibrations.

5.4. Influence of the structural parameters

In this section, the structural parameters of the XSSIP system will be studied when the end-effector of spacecraft is subjected to an impulsive force. Acceleration is referred to as the most important indicator for evaluating the vibration isolation performance. It is noted that the effects of the different structural parameters are studied in the x direction and more details about the case in the z direction will not be presented

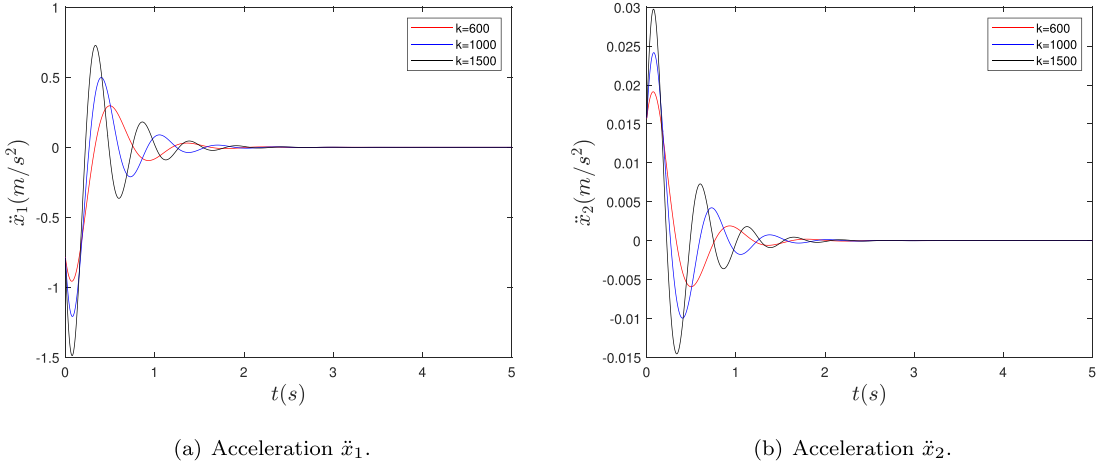


Fig. 25. Acceleration histories with different spring stiffness.

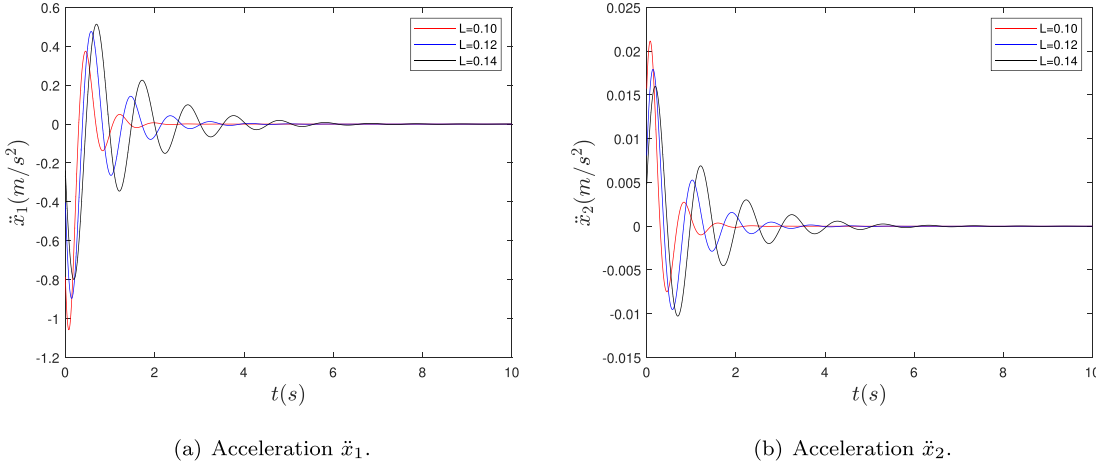
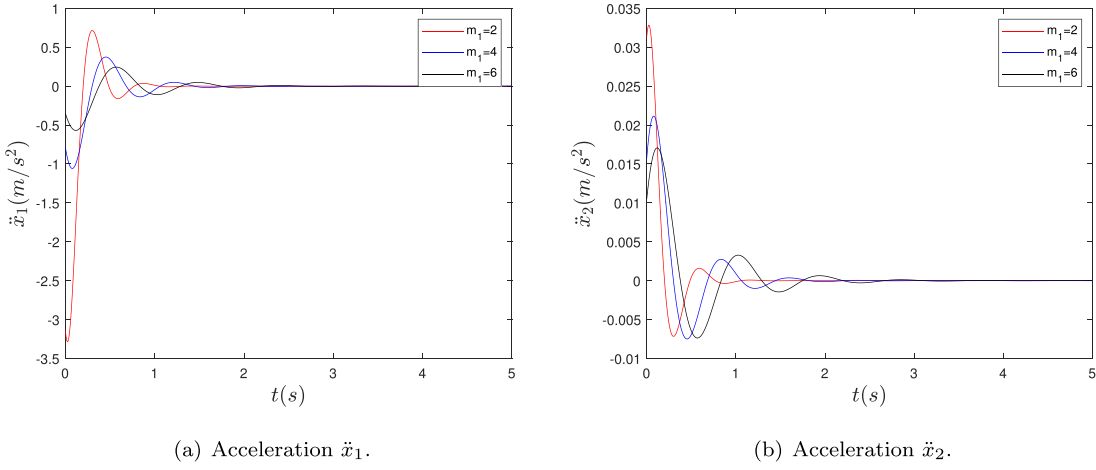


Fig. 26. Acceleration histories with different rod length.

Fig. 27. Acceleration histories with different m_1 .

here.

5.4.1. Effect of the spring stiffness

The influences of spring stiffness on the vibration isolation performance are investigated in Fig. 25. It can be seen from this figure that

increasing the spring stiffness raises the acceleration amplitude of the capture mechanism and the satellite platform. Besides, a larger k of the XSSIP system can lead to more time taken to achieve stability. Therefore, decreasing the spring stiffness k is beneficial to enhance the vibration isolation performance of the XSSIP system.

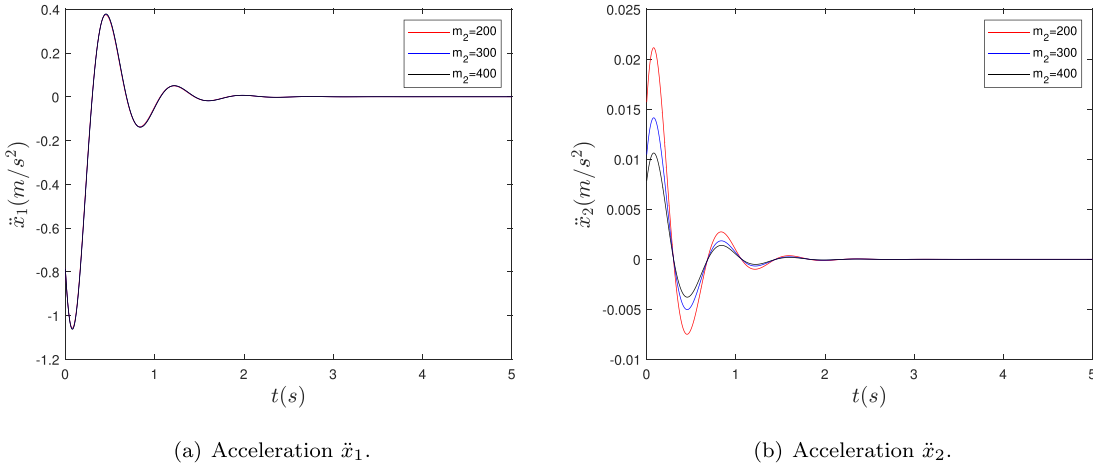
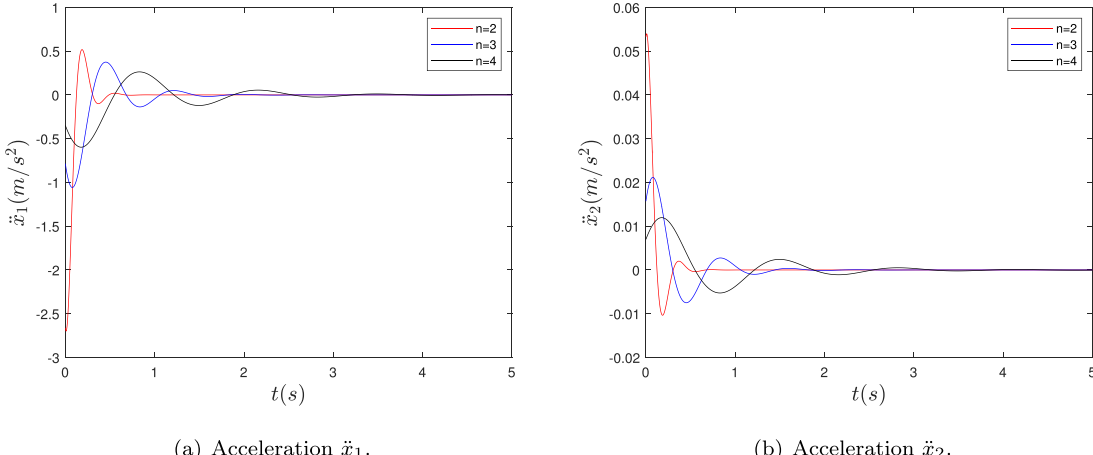
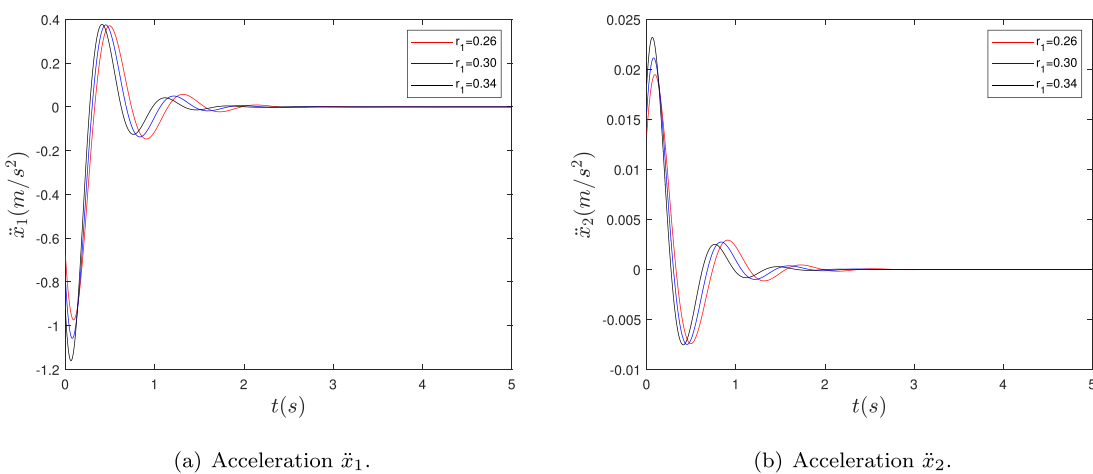
Fig. 28. Acceleration histories with different m_2 .

Fig. 29. Acceleration histories with different layer number.

Fig. 30. Acceleration histories with different radius of Stewart platform r_1 .

5.4.2. Effect of the rod length

Fig. 26 shows the acceleration curves of the two masses with different length of the supporting rod. The rod length in the X-shape structure is chosen as 0.10, 0.12 and 0.14. It can be seen explicitly that increasing the rod length L leads to the increase of vibration

acceleration amplitude and the decay time simultaneously. Therefore, a relative smaller L is beneficial to the better vibration isolation performance of the XSSIP system when subjected to an impulsive force.

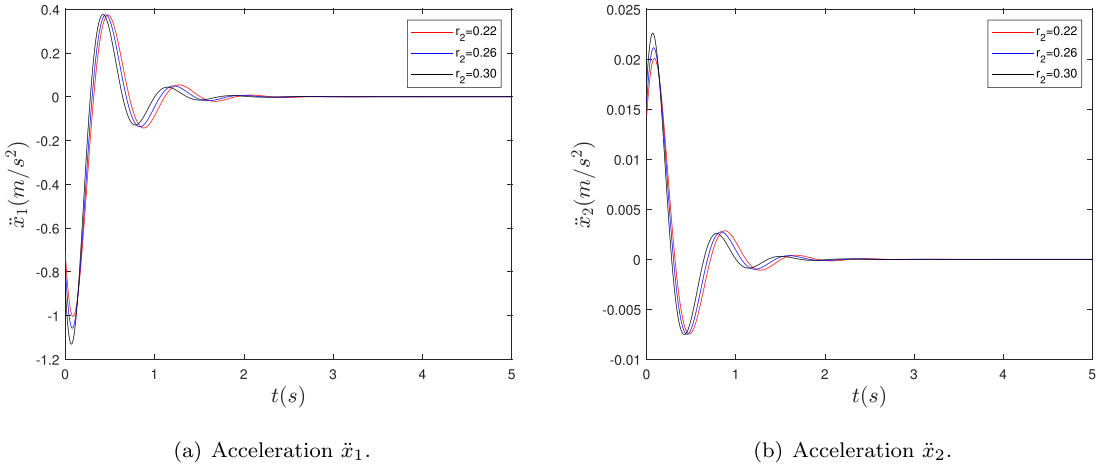
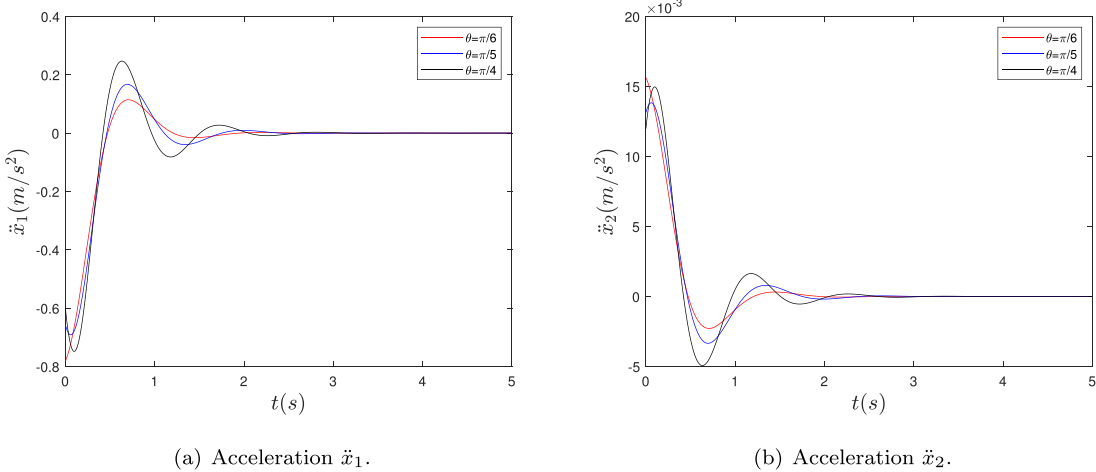
Fig. 31. Acceleration histories with different radius of Stewart platform r_2 .

Fig. 32. Acceleration histories with different assembly angle.

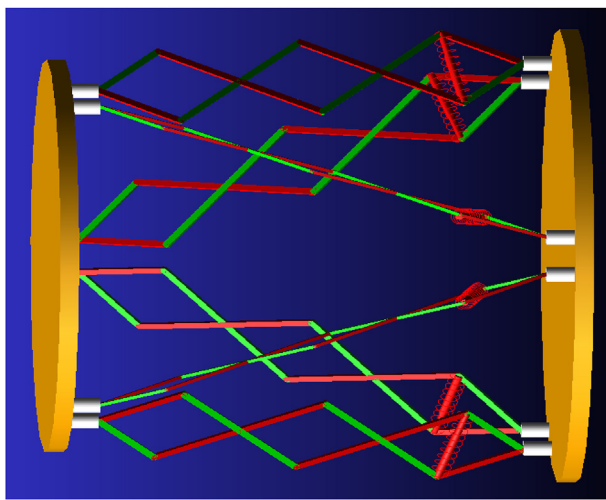


Fig. 33. The XSSIP system built by ADAMS.

5.4.3. Effect of the masses

In the XSSIP system, the masses with respect to m_1 and m_2 play an important role in the vibration isolation performance. The effects on the acceleration of two masses with different m_1 and m_2 are depicted in

Figs. 27 and 28, respectively. For m_1 , increasing the mass m_1 can reduce the amplitude of vibration acceleration and thus the displacement of vibration, which is beneficial to suppress vibrations of spacecraft. Therefore, a larger mass m_1 , that is, a heavier capture mechanism is helpful to achieve the better vibration isolation performance. For m_2 , we can clearly find that changing m_2 has no apparent influence on the acceleration of the capture mechanism. On the other hand, the vibration isolation performance of the satellite platform benefits from a larger m_2 . As we can see from this figure, the larger the mass m_2 is, the smaller the amplitude of vibration about the satellite platform becomes, which represents the better vibration isolation performance of the XSSIP system subjected to an impulsive force.

5.4.4. Effect of the layer number in the X-shape structure

The layer number of the X-shape structure in the XSSIP system is studied in Fig. 29. It can be seen that increasing n can reduce the acceleration amplitude, which means the smaller displacement of vibration. However, the larger the number n is, the longer the decay time becomes. Therefore, we can conclude that increasing the layer number of the X-shape structure can suppress the vibrations of the capture mechanism and the satellite platform better, but enlarge the decay time to achieve stability.

5.4.5. Effect of the radius of the Stewart platform

The Stewart platform plays a significant role as a part of the XSSIP

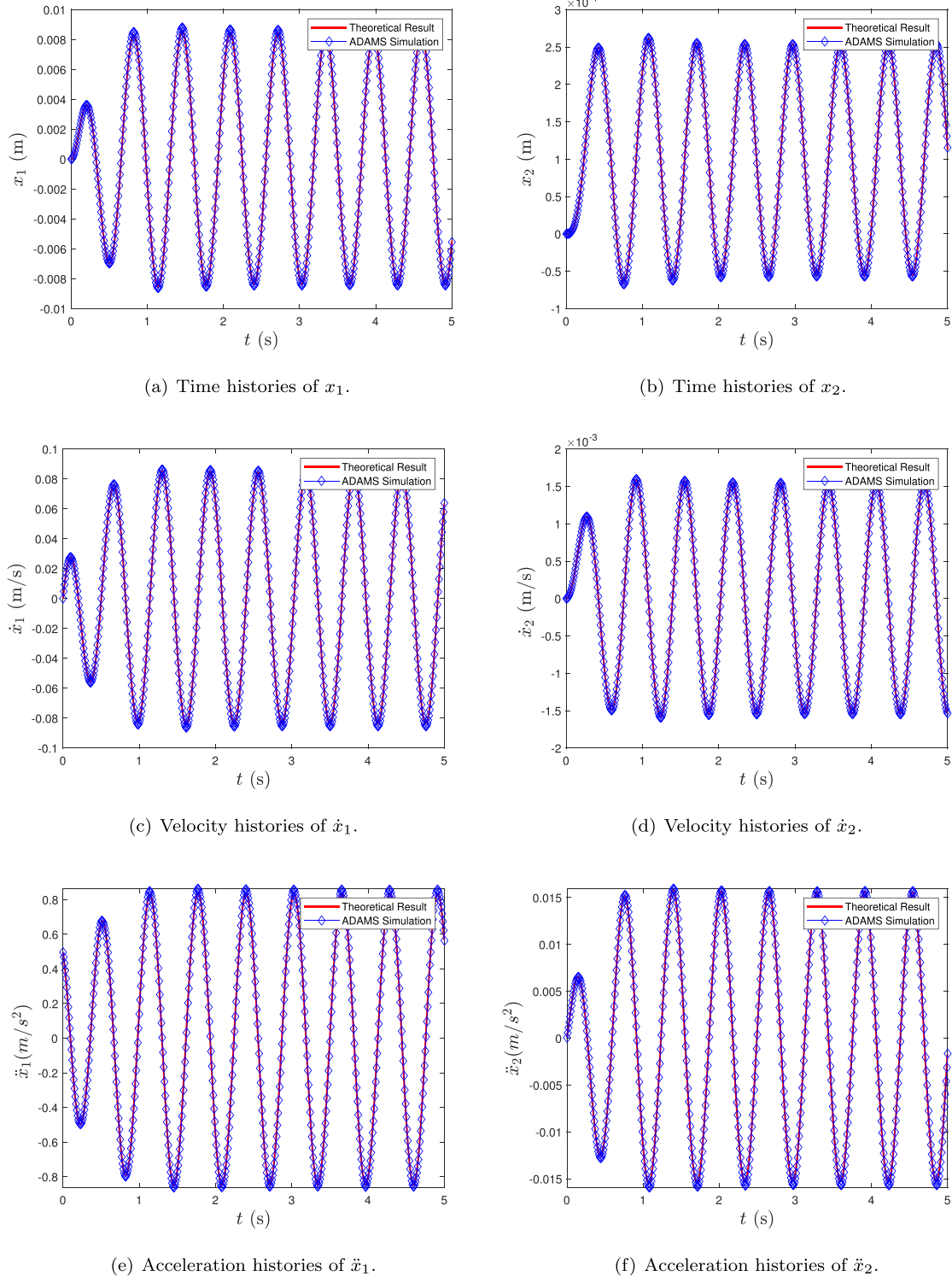


Fig. 34. Verification by ADAMS in the x direction subjected to the periodic external excitation.

system. The vibration isolation performance of the XSSIP system depends on the radius of the Stewart platform to a large extent. The effects on the acceleration of system with different radius of two platforms r_1 and r_2 are displayed in Figs. 30 and 31, respectively. For r_1 , increasing r_1 can lead to the increase of the maximum acceleration, but shorten the decay time to achieve stability. Otherwise, the larger the radius r_1 is, the lower the displacement of the capture mechanism becomes. It means that a larger r_1 is helpful to vibration isolation of the XSSIP system. For

r_2 , the responses of two masses are similar with that in terms of r_1 . It can be seen clearly that decreasing r_2 results in reducing the maximum acceleration of the capture mechanism and the satellite platform. A larger r_2 corresponds to a smaller displacement of two masses. Therefore, increasing r_2 is beneficial to improve the vibration isolation performance of the XSSIP system.

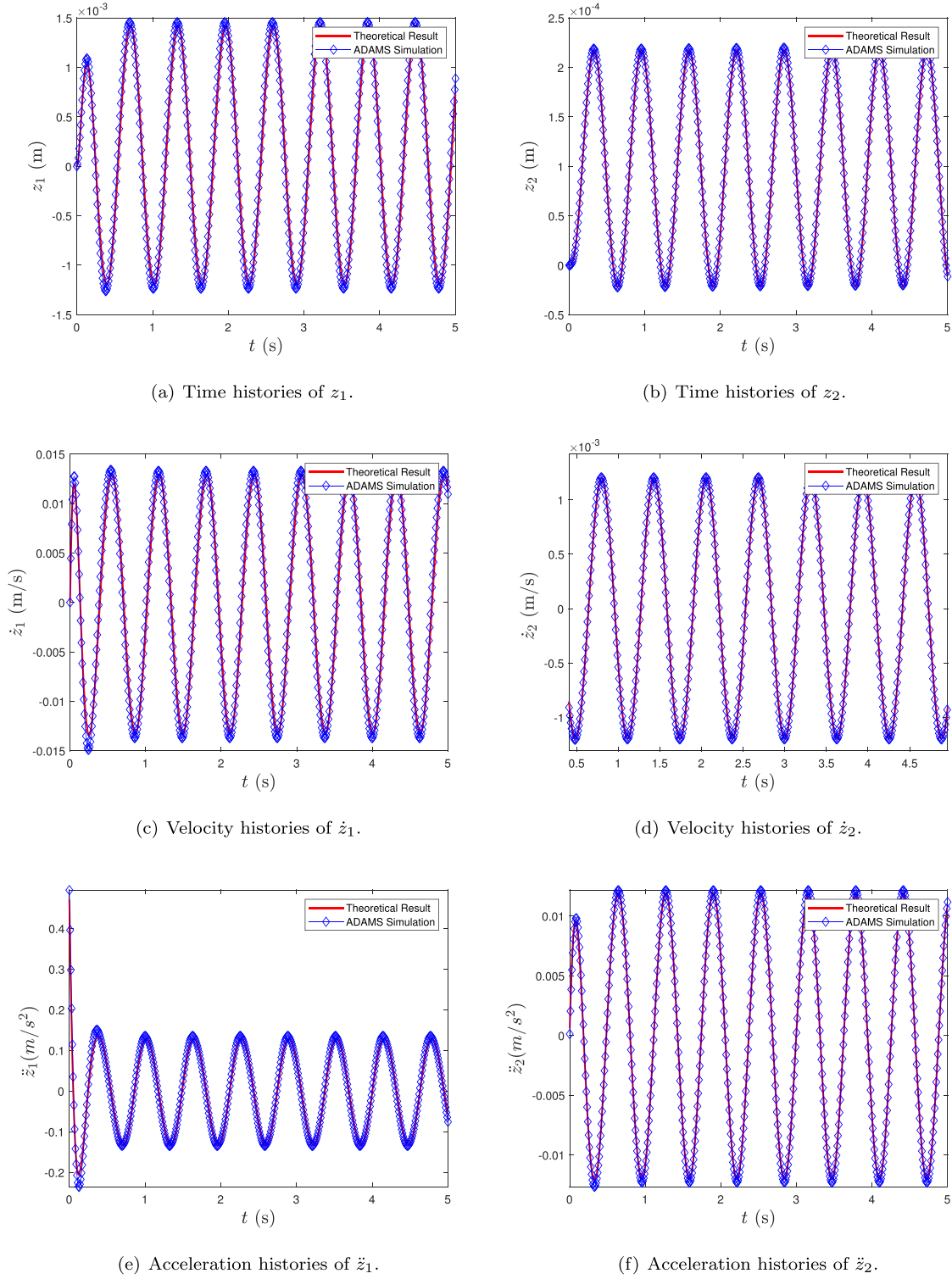


Fig. 35. Verification by ADAMS in the z direction subjected to the periodic external excitation.

5.4.6. Effect of the assembly angle of connecting rods

The acceleration curves for different assembly angles $\theta = \pi/4, \pi/5$ and $\pi/6$ are shown in Fig. 32, respectively. It can be seen that increasing θ leads to the larger vibration acceleration amplitude and extends the decay time. Otherwise, decreasing θ results in a larger acceleration for both the capture mechanism and the satellite platform, which is undesired. Therefore, a larger assembly angle θ is helpful to suppress the vibrations subjected to an impulsive force.

6. Experimental verification by ADAMS

In this section, ADAMS is used to verify the vibration isolation performance of the XSSIP system when it is subjected to the impact or periodic external excitations. The dynamical model built in ADAMS is as shown in Fig. 33 and the structural parameters of the 3-layer X-shape structure are as follows: the length of rod $L = 100$ mm, the assembly angle $\theta = 60^\circ$, the layer number $n = 3$, the friction coefficient of joint

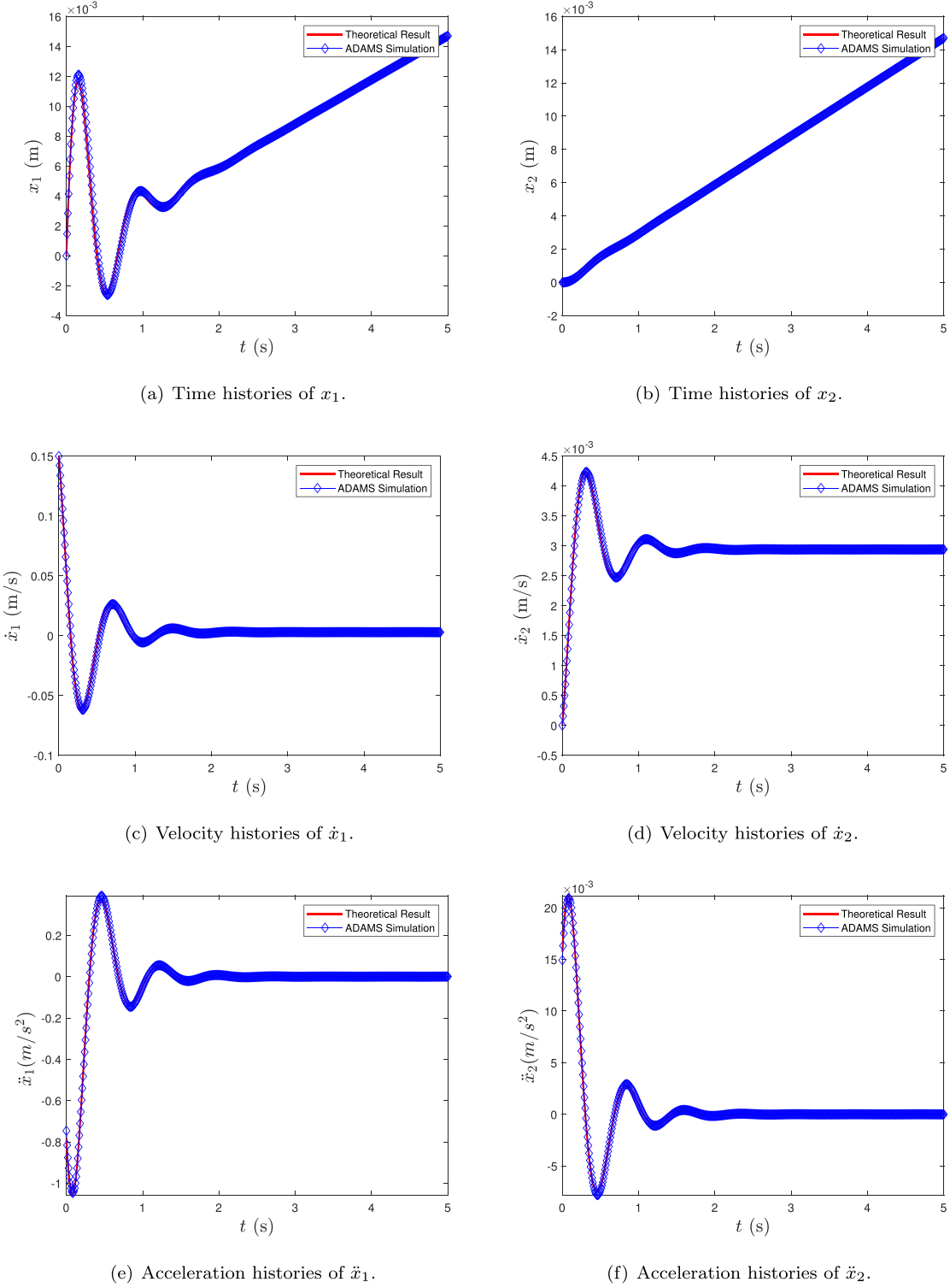


Fig. 36. Verification by ADAMS in the x direction subjected to an impulse.

$c = 0.1 \text{ N}\cdot\text{s}/\text{m}$ and the stiffness coefficient of spring $k = 1.0 \text{ N}/\text{mm}$. The radii of two platforms in the Stewart platform are $r_1 = 300 \text{ mm}$ and $r_2 = 260 \text{ mm}$. The masses of the two platforms are $m_1 = 4 \text{ kg}$ and $m_2 = 200 \text{ kg}$. The damping coefficients in three directions are $c_i = 0.2 \text{ N}\cdot\text{s}/\text{m}$ ($i = 1, 2, 3$). Otherwise, the masses of rods and joints are always neglected in that they are much lighter than the platforms and then all of them are set as $m = 1.0 \times 10^{-6} \text{ kg}$.

6.1. The XSSIP system subjected to the periodic external excitation

In this part, the vibration isolation performance of the XSSIP system is verified in the case that the end-effector of spacecraft, that is, the right platform of the XSSIP system, is subjected to the periodic external excitation arose from the moving payloads mounted on the target. The theoretical analysis and numerical simulations have been given in section 3 and section 4 in details. The periodic external excitation is

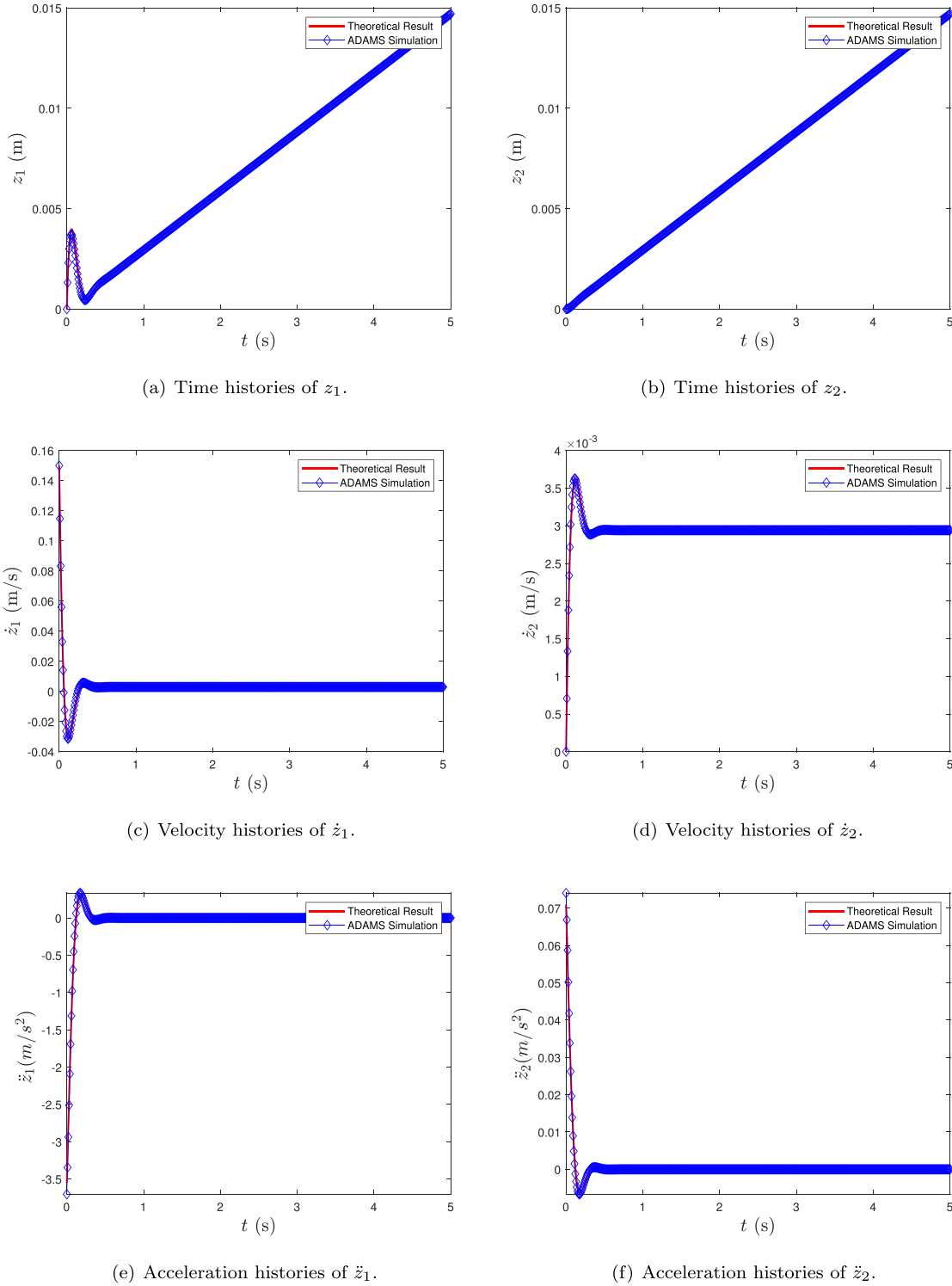


Fig. 37. Verification by ADAMS in the z direction subjected to an impulse.

attached to the right platform of the XSSIP system. In the ADAMS simulation, the periodic excitation force is set as $F = A \cos \omega t$, where $A = 2$ N, $\omega = 10$ rad/s. In this case, the displacement, velocity and acceleration curves in the x and z directions can be acquired by ADAMS simulation. The responses of the XSSIP system by ADAMS simulation in the x direction are shown in Fig. 34 and those in the z direction are depicted in Fig. 35, respectively. From Figs. 34 and 35, responses of the XSSIP system in both directions between the theoretical results and the

ADAMS simulation ones are exactly same on the whole. The amplitudes of m_2 of displacement, velocity and acceleration are remarkably reduced than those of m_1 , which denotes the better vibration isolation performance of the XSSIP system when subjected to the periodic external excitation. Therefore, the theoretical results in the preceding section are well verified to be right and appropriate by ADAMS simulation under this circumstance.

6.2. The XSSIP system subjected to the impact external excitation

Next, we verify the vibration isolation performance of the XSSIP system when the end-effector of spacecraft, that is, the right platform of the XSSIP system, is subjected to the impact excitation due to collision with the targets. The theoretical analysis and numerical results have been given in section 3 and section 5 detailedly. The initial impact external excitation is imposed to the right platform of the XSSIP system. In the ADAMS simulation, the impulse is set as $I = 0.6 \text{ kg}\cdot\text{m}/\text{s}$. Under this circumstance, the displacement, velocity and acceleration curves in the x and z directions can be achieved by ADAMS simulation. The responses of the XSSIP system in the x direction are shown in Fig. 36 and those in the z direction by ADAMS simulation are depicted in Fig. 37, respectively. From Figs. 36 and 37, responses of the XSSIP system in both directions between the theoretical results and the ADAMS simulation ones are exactly same on the whole. The amplitudes of m_2 in displacement, velocity and acceleration curves are remarkably reduced than those of m_1 , which denotes the better vibration isolation performance of the XSSIP system when subjected to an impulse. Therefore, the theoretical results are well verified to be right and appropriate by ADAMS in this case.

7. Conclusion

A novel X-shape structure-based Stewart isolation platform system, abbreviated as the XSSIP system, is first proposed to install between the capture mechanism and the robotic arm of a free-floating spacecraft. It can suppress the post-capture vibrations when the end-effector is subjected to the periodic and impulsive external excitations carrying out the on-orbit capture missions. The dynamic equations in space microgravity environment are established differing from the traditional ground vibration isolation system. The vibration isolation performances of the present system are thoroughly investigated under either impulsive or periodic excitation in tangential and normal directions. In addition, influences on the vibration isolation responses with respect to different structural parameters of the XSSIP system are studied in detail. In this work, the proposed XSSIP system possesses two advantages: 1) It can achieve the multi-direction vibration isolation performance when the end-effector is subjected to the external periodic or impulsive excitations. 2) It has a significant superiority over the Stewart platform system based on the traditional SMD isolator and a better prospect of application in aerospace engineering. Finally, the ADAMS simulations are conducted to verify the validity and accuracy of the XSSIP model.

Acknowledgments

This work is supported by National Natural Science Foundation of China (11972026) and funded by the CAS Youth Innovation Promotion Association as an invited member.

References

- [1] J. Zhang, D. Li, M.J. Chen, S. Dong, An ultra-low frequency parallel connection nonlinear isolator for precision instruments, *Key Eng. Mater.* 257 (2004) 231–238.
- [2] M. Li, Y. Zhang, Y. Wang, Q. Hu, R. Qi, The pointing and vibration isolation integrated control method for optical payload, *J. Sound Vib.* 438 (2019) 441–456.
- [3] W.S. Robertson, M. Kidner, B.S. Cazzolato, A.C. Zander, Theoretical design parameters for a quasi-zero stiffness magnetic spring for vibration isolation, *J. Sound Vib.* 326 (1–2) (2009) 88–103.
- [4] L. Liu, G. Zheng, W. Huang, Octo-strut vibration isolation platform and its application to whole spacecraft vibration isolation, *J. Sound Vib.* 289 (4–5) (2006) 726–744.
- [5] Y. Zhang, C. Sheng, Z. Guo, Y. Wang, W. Li, Dynamic characteristics and performance evaluation for the part strut failure of the vibration isolation platform on satellites, *Acta Astronaut.* 133 (2017) 403–415.
- [6] E. Stoll, J. Letschnik, U. Walter, J. Artigas, P. Kremer, C. Preusche, G. Hirzinger, On-orbit servicing, *IEEE Robot. Autom. Mag.* 16 (4) (2009) 29–33.
- [7] A. Badawy, C.R. McInnes, On-orbit assembly using superquadric potential fields, *J. Guid. Control Dyn.* 31 (1) (2008) 30–43.
- [8] J.H. Saleh, E.S. Lamassouire, D.E. Hastings, D.J. Newman, Flexibility and the value of on-orbit servicing: new customer-centric perspective, *J. Spacecr. Rocket.* 40 (2) (2003) 279–291.
- [9] A. Flores-Abad, O. Ma, K. Pham, S. Ulrich, A review of space robotics technologies for on-orbit servicing, *Prog. Aerosp. Sci.* 68 (2014) 1–26.
- [10] A. Long, M. Richards, D.E. Hastings, On-orbit servicing: a new value proposition for satellite design and operation, *J. Spacecr. Rocket.* 44 (4) (2007) 964–976.
- [11] C. Kaiser, F. Sjöberg, J.M. Delcura, B. Eilertsen, Smart-olev—an orbital life extension vehicle for servicing commercial spacecrafts in geo, *Acta Astronaut.* 63 (1–4) (2008) 400–410.
- [12] T. Debus, S. Dougherty, Overview and performance of the front-end robotics enabling near-term demonstration (frend) robotic arm, *AIAA Infotech Aerospace Conference and AIAA Unmanned... Unlimited Conference*, 2009, p. 1870.
- [13] X. Du, B. Liang, W. Xu, Y. Qiu, Pose measurement of large non-cooperative satellite based on collaborative cameras, *Acta Astronaut.* 68 (11–12) (2011) 2047–2065.
- [14] S.-I. Nishida, S. Kawamoto, Y. Okawa, F. Terui, S. Kitamura, Space debris removal system using a small satellite, *Acta Astronaut.* 65 (1–2) (2009) 95–102.
- [15] C. Xavier, K. Sun-Wook, I. Michel, M. Arun, J. Gilbert, Post-impact dynamics of two multi-body systems attempting docking/berthing, *Acta Astronaut.* 40 (11) (1997) 759–769.
- [16] X. Cyril, A.K. Misra, M. Ingham, G.J. Jaar, Postcapture dynamics of a spacecraft-manipulator-payload system, *J. Guid. Control Dyn.* 23 (1) (2000) 95–100.
- [17] H. Dai, X. Jing, Y. Wang, X. Yue, J. Yuan, Post-capture vibration suppression of spacecraft via a bio-inspired isolation system, *Mech. Syst. Signal Process.* 105 (2018) 214–240.
- [18] H. Dai, X. Jing, C. Sun, Y. Wang, X. Yue, Accurate modeling and analysis of a bio-inspired isolation system: with application to on-orbit capture, *Mech. Syst. Signal Process.* 109 (2018) 111–133.
- [19] X. Sun, X. Jing, J. Xu, L. Cheng, Vibration isolation via a scissor-like structured platform, *J. Sound Vib.* 333 (9) (2014) 2404–2420.
- [20] Z. Wu, X. Jing, J. Bian, F. Li, R. Allen, Vibration isolation by exploring bio-inspired structural nonlinearity, *Bioinspiration Biomim.* 10 (5) (2015) 056015.
- [21] C. Liu, X. Jing, F. Li, Vibration isolation using a hybrid lever-type isolation system with an x-shape supporting structure, *Int. J. Mech. Sci.* 98 (2015) 169–177.
- [22] X. Sun, X. Jing, A nonlinear vibration isolator achieving high-static-low-dynamic stiffness and tunable anti-resonance frequency band, *Mech. Syst. Signal Process.* 80 (2016) 166–188.
- [23] D. Stewart, A platform with six degrees of freedom, *Proc. Inst. Mech. Eng.* 180 (1) (1965) 371–386.
- [24] Z.J. Geng, L.S. Haynes, Six degree-of-freedom active vibration control using the stewart platforms, *IEEE Trans. Control Syst. Technol.* 2 (1) (1994) 45–53.
- [25] Z. Wu, X. Jing, B. Sun, F. Li, A 6d of passive vibration isolator using x-shape supporting structures, *J. Sound Vib.* 380 (2016) 90–111.
- [26] G. Hauge, M. Campbell, Sensors and control of a space-based six-axis vibration isolation system, *J. Sound Vib.* 269 (3–5) (2004) 913–931.
- [27] A. Preumont, M. Horodinca, I. Romanescu, B. De Marneffe, M. Avraam, A. Deraemaeker, F. Bossens, A.A. Hanieh, A six-axis single-stage active vibration isolator based on stewart platform, *J. Sound Vib.* 300 (3–5) (2007) 644–661.
- [28] M.E. Hoque, T. Mizuno, Y. Ishino, M. Takasaki, A six-axis hybrid vibration isolation system using active zero-power control supported by passive weight support mechanism, *J. Sound Vib.* 329 (17) (2010) 3417–3430.
- [29] M.E. Hoque, T. Mizuno, Y. Ishino, M. Takasaki, A three-axis vibration isolation system using modified zero-power controller with parallel mechanism technique, *Mechatronics* 21 (6) (2011) 1055–1062.
- [30] K.K. Denoyer, R.S. Erwin, R.R. Ninneman, Advanced smart structures flight experiments for precision spacecraft, *Acta Astronaut.* 47 (2–9) (2000) 389–397.
- [31] Y. Xu, H. Liao, L. Liu, Y. Wang, Modeling and robust h-infinite control of a novel non-contact ultra-quiet stewart spacecraft, *Acta Astronaut.* 107 (2015) 274–289.
- [32] Y. Kong, H. Huang, Vibration isolation and dual-stage actuation pointing system for space precision payloads, *Acta Astronaut.* 143 (2018) 183–192.